NUCLEAR SCIENCE AND ENGINEERING: **131**, 293–328 (1999)

Cross-Section Evaluations to 150 MeV for Accelerator-Driven Systems and Implementation in MCNPX

M. B. Chadwick,* P. G. Young, S. Chiba,† S. C. Frankle, G. M. Hale, H. G. Hughes, A. J. Koning,‡
R. C. Little, R. E. MacFarlane, R. E. Prael, and L. S. Waters

Los Alamos National Laboratory, Los Alamos, New Mexico 87545

Received April 24, 1998
Accepted July 30, 1998

Abstract—*New accelerator-driven technologies that utilize spallation neutrons, such as the production of tritium and the transmutation of radioactive waste, require accurate nuclear data to model the performance of the target/blanket assembly and to predict neutron production, activation, heating, shielding requirements, and material damage. To meet these needs, nuclear-data evaluations and libraries up to 150 MeV have been developed for use in transport calculations to guide engineering design. By using advanced nuclear models that account for details of nuclear structure and the quantum nature of the nuclear scattering, significant gains in accuracy can be achieved below 150 MeV, where intranuclear cascade calculations become less accurate. Evaluations are in ENDF-6 format for important target/blanket and shielding materials (isotopes of H, C, N, O, Al, Si, P, Ca, Cr, Fe, Ni, Cu, Nb, W, Hg, and Pb) for both incident neutrons and incident protons. The evaluations are based on measured data as well as predictions from the GNASH nuclear model code, which calculates cross sections using Hauser-Feshbach, exciton, and Feshbach-Kerman-Koonin preequilibrium models. Elastic scattering distributions and direct reactions are calculated from the optical model. All evaluations specify production cross sections and energy-angle correlated spectra of secondary light particles as well as production cross sections and energy distributions of heavy recoils and gamma rays. A formalism developed to calculate recoil energy distributions is presented. The use of these nuclear data in the MCNPX radiation transport code is also briefly described. This code merges essential elements of the LAHET and MCNP codes and uses these new data below 150 MeV and intranuclear cascade collision physics at higher energies. Extensive comparisons are shown between the evaluated results and experimental cross-section data to benchmark and validate the evaluated library. In addition, integral benchmarks of calculated and measured kerma coefficients for neutron energy deposition and neutron transmission through an iron slab compared with MCNPX calculations are provided. These evaluations have been accepted into the ENDF/B-VI library as Release 6.*

I. INTRODUCTION

High-current proton accelerators are being designed at Los Alamos National Laboratory (LANL) and other laboratories for accelerator production of tritium (APT), transmuting long-lived radioactive waste into shorter-lived products [accelerator transmutation of waste (ATW)], converting excess plutonium, and producing energy. These technologies make use of spallation neutrons produced in (p, xn) and (n, xn) nuclear reactions on high-Z targets. New nuclear cross-section data are needed to improve theoretical predictions of neutron production, shielding requirements, activation, radiation heating, and materials damage. Such predictions can guide the design of the target/blanket configurations and can reduce engineering overdesign costs.

To address these needs, a program is under way to develop new evaluated nuclear data libraries for incident protons and neutrons up to 150 MeV for a range of

*E-mail: mbchadwick@lanl.gov

†Permanent address: Advanced Sciences Research Center, JAERI, Tokai, Ibaraki 319-11, Japan.

‡Permanent address: ECN, P.O. Box 1, 1755 ZG Petten, The Netherlands.

high-priority elements[a] in the ENDF-6 format.[2,3] These evaluations are based on a combination of nuclear model calculations and measured data to evaluate cross sections. The MCNP radiation transport code[4] is being developed to utilize these evaluated libraries, as well as to include charged-particle transport, and is being merged with the LAHET intranuclear cascade code[5] for modeling nuclear reactions above 150 MeV. The extended merged code is referred to as MCNPX (Ref. 6). This paper describes methods and results of the neutron and proton cross-section evaluations and briefly summarizes their implementation in the MCNPX code.

Since the APT program has been the primary source of support for this research, the evaluations described here are for high-priority elements in that program: H, C, N, O, Al, Si, P, Ca, Cr, Fe, Ni, Cu, Nb, W, and Pb, as well as for Hg, owing to its importance as a spallation target for neutron-scattering material science studies. While these elements are also likely to be of high priority in other accelerator-driven applications, there are some notable omissions in this work, such as actinides. Future research is needed, therefore, to extend the usefulness of this work for ATW applications. In the case of tritium production, the current design consists of a 1.7-GeV proton beam incident on a split tungsten target surrounded by a lead blanket. Through (p,xn) and (n,xn) nuclear reactions, neutrons are produced and are moderated by heavy water in the target region and light water in the blanket region. These moderated neutrons are subsequently captured on ^{3}He, which flows throughout the blanket system, to produce tritium via the (n,p) reaction.

The GNASH nuclear model reaction code[7,8] is used extensively in this work to predict nuclear reaction cross sections for particle and gamma-ray emission because measured data at higher energies are relatively sparse. However, extensive use is made of existing experimental data to guide and benchmark the model calculations, and numerous comparisons between the evaluated results and experimental data are shown in this paper for validation purposes. Furthermore, the evaluated data for the total cross sections and the total nonelastic cross sections are usually primarily determined from measurements, since there are often a sufficient number of such experimental data to constrain the evaluations. An evaluation based on experimental data, in addition to nuclear model predictions, can be expected to be more accurate than that based solely on model calculations. The optical model codes ECIS (Ref. 9) and SCAT (Ref. 10) were used to predict elastic scattering angular distributions. Full details of the calculation and evaluation methods used are described in Sec. II.

[a]The new 150-MeV evaluated cross sections, collectively referred to as the LA150 library, are available via the internet at http://t2.lanl.gov/data/he.html. They can be augmented with other evaluations (e.g., ^{9}Be and ^{238}U) to 100 MeV developed in the late 1980s by Young et al.[1]

The LAHET Code System has been instrumental in guiding the design of spallation targets. Until now, the LAHET intranuclear cascade code has been used to model the nuclear interactions as well as the radiation transport for neutral particles above 20 MeV and for charged particles of all energies. Below 20 MeV, the nuclear reactions and the transport of neutral particles are performed by the MCNP code,[4] which uses ENDF/B-VI-evaluated nuclear data libraries. The intranuclear cascade model in LAHET is most accurate above 150 MeV, where semiclassical approximations become more applicable. Below 150 MeV, however, nuclear interactions are more sensitive to specific details of nuclear structure along with quantum effects in the scattering. For this reason, the evaluated data libraries are being extended up to higher energies (150 MeV), since the libraries can be based on the GNASH, ECIS, and SCAT nuclear modeling codes, which better account for this physics.

The upper data-library energy of 150 MeV was chosen for the following reasons:

1. It corresponds approximately to the pion threshold, and pion production is not included in the GNASH model code used to evaluate the cross sections.

2. The INC model works fairly well above this energy.

3. The GNASH code system has been benchmarked extensively below this energy and has been shown to perform well in an international code intercomparison,[11] but for use at higher energies, additional improvements would be desirable, such as including more than two multiple preequilibrium particles.[12,13]

A summary of the information included in the ENDF evaluations is given in Table I. For incident neutrons, the new evaluations to 150 MeV have been built on the existing ENDF/B-VI evaluations, which usually extend up to 20 MeV. For protons, the new evaluations extend from 1 to 150 MeV. Total, nonelastic, and elastic scattering cross sections are given, as are production cross sections for light particles and heavy nuclides. For the light particles, angle-integrated production spectra (inclusive emission spectra) are tabulated along with the preequilibrium fractions to allow angle-energy correlated double-differential emission spectra to be determined. For heavy nuclides (recoils) and gamma rays, only angle-integrated emission spectra are provided, and isotropic angular distributions are assumed. For gamma rays, this is a reasonable approximation; for recoils, the angular distributions are unimportant for most applications due to the very small recoil ranges.

Figures 1 and 2 provide three-dimensional illustrative examples of the emission spectra information available from the evaluations. These examples, for neutrons incident on lead and on carbon from 20 to 150 MeV, were obtained by combining the nonelastic cross sections,

TABLE I

Contents of LA150 Data Library for Incident Neutrons and Protons

Reaction Type	Cross Section	Angle-Integrated Emission Spectra	Angle-Energy-Correlated Emission Spectra
Total	Yes (for neutrons)	– – –	– – –
Nonelastic	Yes	– – –	– – –
Elastic	Yes	– – –	(c.m. angular distributions)
Neutron production	Yes	Yes, in c.m.	Yes, using Kalbach preequilibrium ratios
Proton production	Yes	Yes, in c.m.	Yes, using Kalbach preequilibrium ratios
Deuteron production	Yes	Yes, in c.m.	Yes, using Kalbach preequilibrium ratios
Alpha production	Yes	Yes, in c.m.	Yes, using Kalbach preequilibrium ratios
Triton production	Yes	Yes, in c.m.	Yes, using Kalbach preequilibrium ratios
Gamma Production	Yes	Yes, in lab	No (isotropy assumed)
Nuclide production	Yes	Yes, recoils in lab	No (isotropy assumed)

multiplicities (yields), and probability energy distributions tabulated in the ENDF file. Figure 1 shows the emission spectra of the light ejectiles and gamma rays and the trends of increasing high-energy preequilibrium emission with increasing incident energy. The effect of the Coulomb barrier in suppressing low-energy charged-particle emission is also evident. (The low-energy evaporation peaks seen for tritons and alphas are significantly smaller than those for protons—they appear pronounced in Fig. 1 due to the smaller cross-section scales used in the graphs and the small magnitude of cluster preequilibrium emission.) In Fig. 2 the recoil spectra are shown for only a few of the many product nuclides formed for neutrons on carbon. The heavier mass of the recoil nuclides results in the extension of their emission energies to lower values than seen for the light particles in Fig. 1 (note that the emission energy axes in Fig. 2 only extend to 15 MeV, unlike those in Fig. 1 that extend to 150 MeV). Three-dimensional pictures of this type, along with similar pictures of the preequilibrium ratio (used for obtaining angular distributions) and of light-particle production cross sections, are shown for every isotope evaluation in a laboratory report.[2] They provide an important component to the validation of the evaluations because trends in the large amounts of evaluated data can be quickly observed.

Prior to the present work, high-energy neutron and proton data libraries up to 100 MeV were first developed in the late 1980s for a range of elements.[1] More recently, high-energy libraries were generated for particle radiotherapy simulations in the Lawrence Livermore National Laboratory (LLNL) PEREGRINE project, through an LLNL-LANL collaboration.[14,15] The present evaluated data libraries represent an advance over these earlier works because they also include energy-distribution and yield information for the heavy-recoil product nuclides and are based on the latest version of the GNASH code.[7] In recent years, other groups have initiated programs to develop high-energy nuclear data libraries, mainly for ATW and medical applications.[16–19]

This paper is organized as follows. Section II provides an overview of the nuclear models used in this work. Section III (and the Appendix) discusses the calculation of nuclear recoil spectra, a new capability we have recently developed. Section IV describes the evaluations for each of the elements studied and provides detailed comparisons with experimental cross-section data. Section V describes recent extensions to the MCNP-LAHET code system, as embodied in the new MCNPX code, to utilize the ENDF libraries in the calculations of radiation transport and energy deposition and shows some integral benchmark results that have been obtained to validate the cross-section evaluations.

II. NUCLEAR MODEL CALCULATIONS

II.A. General

The latest version of the GNASH code has been described in Ref. 7, and its recent application in nuclear reaction evaluation work has been described in Refs. 14, 15, and 20. For this reason, here we provide only an overview of the models used in the calculations, concentrating on new features.

The GNASH code calculates nuclear reaction cross sections using the Hauser-Feshbach theory for equilibrium decay and the exciton model for preequilibrium decay. Direct reactions to low-lying residual nucleus states are precalculated and included as input into the GNASH calculations. The preequilibrium emission cross sections can also be calculated according to the quantum mechanical Feshbach-Kerman-Koonin (FKK) theory.[21,22] However, for calculations of the large number of nuclear data needed, the exciton model was generally utilized because of the shorter computational times needed, and

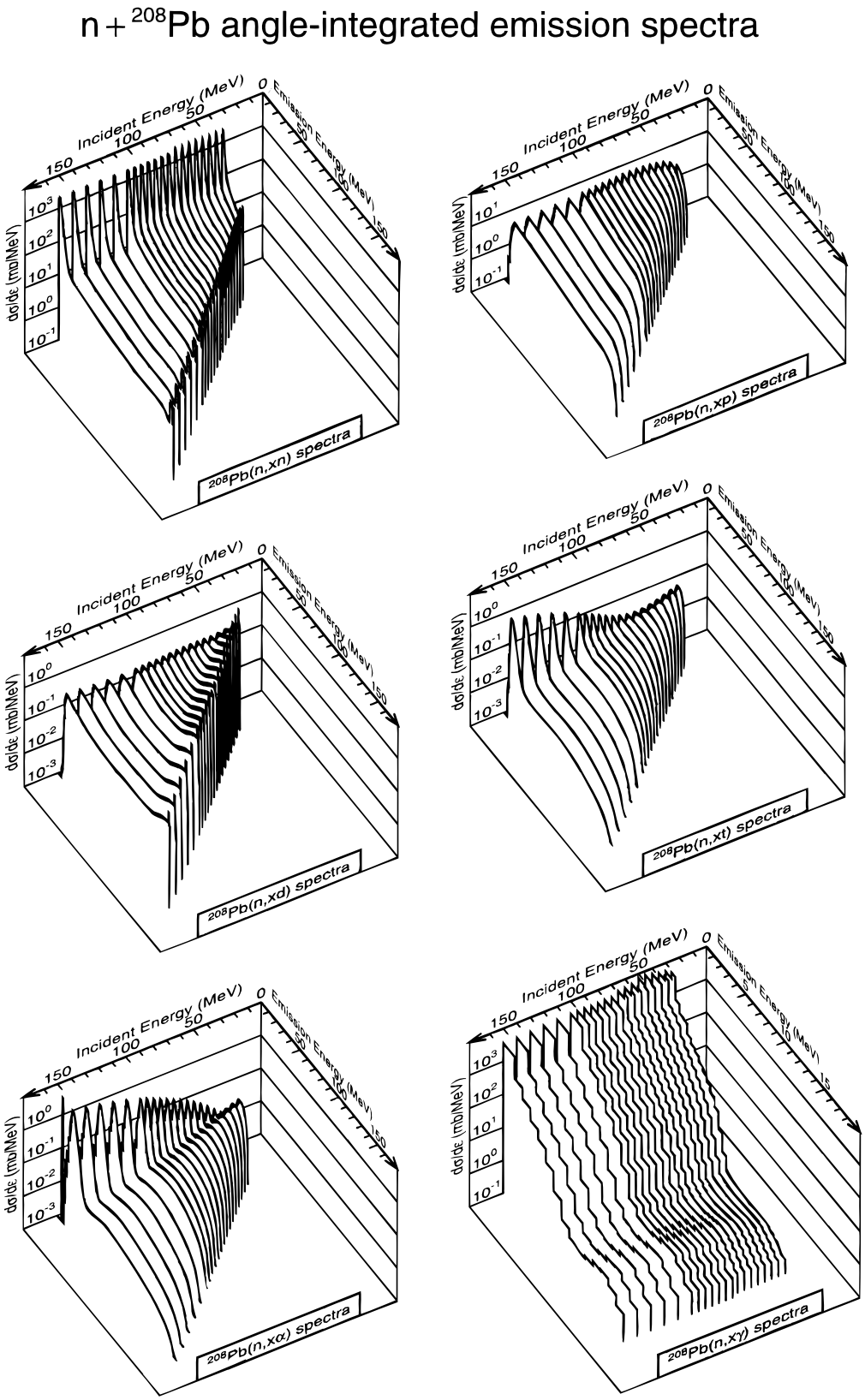

Fig. 1. Three-dimensional graphical representations of light-particle angle-integrated emission spectra from the ENDF evaluation for neutrons on lead. The spectra are in the c.m. reference frame. Pictures of this type are available in Ref. 2 for all isotopes evaluated.

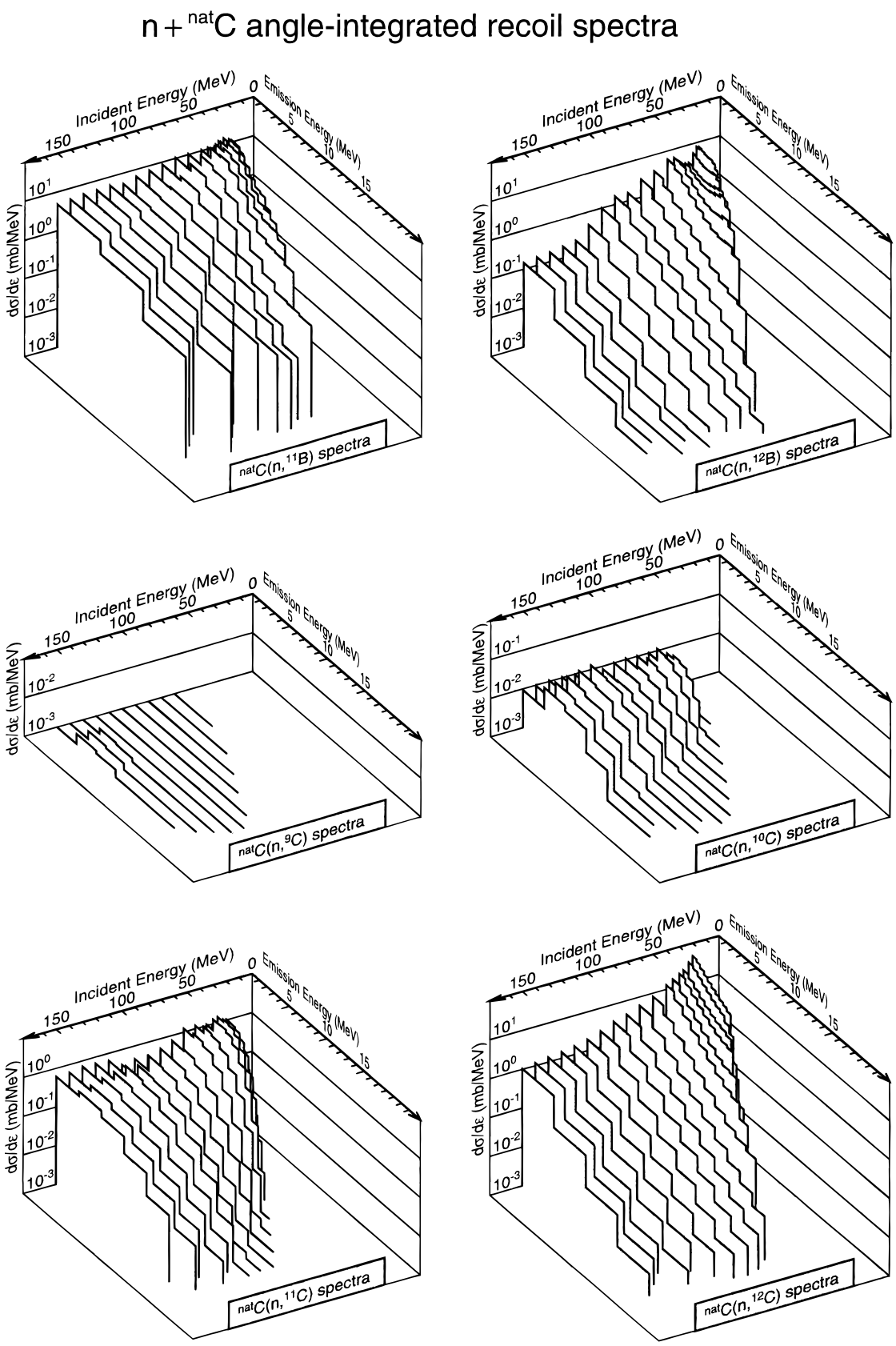

Fig. 2. Three-dimensional graphical representations of recoil angle-integrated emission spectra from the ENDF evaluation for neutrons on carbon. The spectra are in the laboratory reference frame.

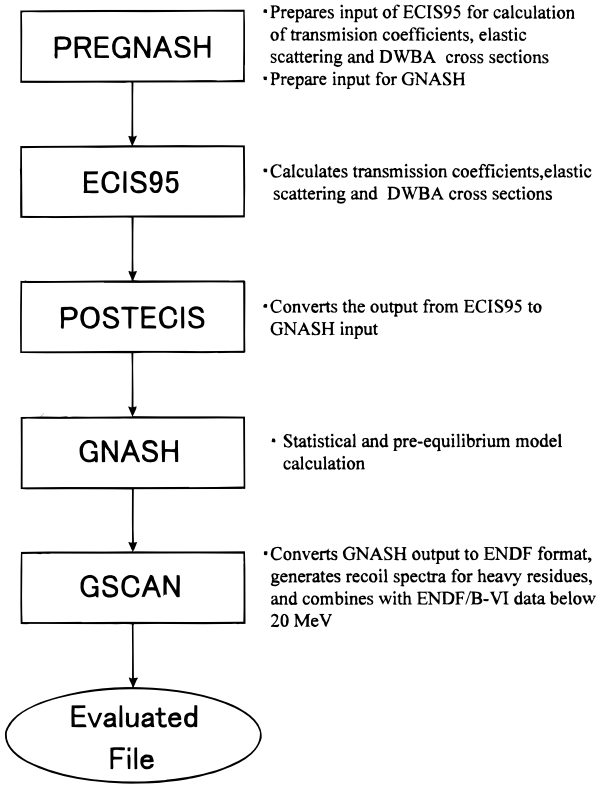

Fig. 3. Schematic flowchart of the computer codes used in the nuclear model calculations.

comparisons with the FKK theory were made only in select cases for validation purposes (see Sec. II.D).

The system of computer codes used to produce the evaluated cross sections is shown in Fig. 3. The steps in the evaluation involve (a) setting up the input information using the PREGNASH code[23]; (b) calculating elastic scattering, transmission coefficients, and direct inelastic scattering with an optical mode code such as ECIS; (c) running GNASH to determine emission cross sections and spectra; and finally (d) running GSCAN, a code that scans the GNASH output, calculates recoil emission spectra for the heavy isotope products, and generates data in ENDF-6 format.

Where secondary particle emission experimental data exist, certain input parameters, such as level density parameters and the preequilibrium matrix element, are sometimes adjusted within their ranges of validity to optimize agreement with the measurements.

Details of the nuclear models used are described in Secs. II.B, II.C, and II.D.

II.B. Optical Models

Evaluations begin with the development, and in some cases selection from the literature, of an optical model (deformed or spherical, depending on the nucleus under study) to describe measured total, reaction, and elastic scattering cross sections. In many cases, if a specific nucleus-dependent potential does not exist, we have made use of a modified version of Madland's global medium-energy nucleon potential[24] above an energy of, typically, 30 to 50 MeV. The revised expression for medium-energy potential is given in Table II, where the symbols are defined in a conventional way. Generally, this global potential gives a good description of measured total and reaction cross sections and elastic scattering distributions up to ~160 MeV. Note that the potential in Table II is a nonrelativistic approximation to that presented in Ref. 24, which uses relativistic kinematics, allowing it to be used in the nonrelativistic SCAT code.

For evaluation of Cr, Ni, and Cu, we have searched for new nucleon optical potentials to reproduce in more detail the isotopic data for elastic scattering angular distributions, *s*-wave strength function[25] and total cross sections for neutron projectiles, and total reaction cross sections for proton projectiles. The parameter search was carried out based on the Bayesian generalized least-squares method for Cr and Ni and by ECISVIEW (Refs. 16 and 26) for Cu. In these cases, the energy dependencies of potential depths are expressed in the

TABLE II

Global Nucleon Optical Potential*

Parameter	Expression
V_R	$105.5 \mp 16.5\eta - 17.14375\ln(E) - 0.4Z/A^{1/3}(\frac{1}{2} + t_z)$
r_R	$1.125 + 0.001E$
a_R	$0.675 + 0.00031E$
W_D	0.0
W_V	$2.4346 + 0.1016E - 9.288 \times 10^{-4}E^2 + 3.87 \times 10^{-6}E^3$
r_V	$1.650 - 0.0024E$
a_V	$0.328 + 0.00244E$
V_{so}	$19.0 \pm 3.75\eta - 3.154\ln(E)$
W_{so}	0.0
r_{so}	$\begin{cases} 0.920 + 0.0305A^{1/3} \\ 0.98\ (A \le 40) \end{cases}$
a_{so}	$0.768 - 0.0012E$
r_c	1.25

*For energies from ~30 to 50 MeV up to 160 MeV, based on Madland's[24] potential but modified for use in a nonrelativistic calculation. The potential depths and projectile energy E are expressed in mega-electron-volts, while the geometric parameters are given in femtometres. The symbol t_z denotes the z component of projectile isospin, i.e., $\frac{1}{2}$ for neutrons and $-\frac{1}{2}$ for protons, $\eta = (N - Z)/A$, where N, Z, and A represent the neutron, proton, and mass numbers of the target nucleus, respectively. In $\mp$ or $\pm$, the upper sign corresponds to neutrons and the lower one to protons.

following way, which is similar to that proposed by Delaroche et al.[27]:

$$V_R = Ve^{-\lambda_R(E-E_F)} + V_0 + V_1 E \ ,$$

$$W_D = W_{D_0} e^{-\lambda_{W_D}(E-E_F)} \frac{(E-E_F)^4}{(E-E_F)^4 + W_{D_1}^4} \ ,$$

$$W_V = W_{V_0} \frac{(E-E_F)^4}{(E-E_F)^4 + W_{V_1}^4} \ ,$$

$$V_{so} = 6.0e^{-0.005E}$$

and

$$W_{so} = 0.2 - 0.011E \ . \quad (1)$$

The symbol E_F denotes the Fermi energy and was calculated as

$$E_F(n) = -\tfrac{1}{2}(S_n(A) + S_n(A+n))$$

and

$$E_F(p) = -\tfrac{1}{2}(S_p(A) + S_p(A+p)) \ , \quad (2)$$

where

$E_F(n)$ = neutron Fermi energy

$E_F(p)$ = proton Fermi energy

$S_n(A)$ = neutron separation energy from target nucleus A

$S_p(A)$ = proton separation energy from target nucleus A

$S_n(A+n)$ = neutron separation energy from target + n nucleus

$S_p(A+p)$ = proton separation energy for target + p nucleus.

The potential form factor was chosen to be of Woods-Saxon form for V_R and W_V, derivative Woods-Saxon for W_D, and Thomas-Fermi form for the spin-orbit parts. The calculation was performed with ECIS making use of relativistic kinematics.

The following global potentials were employed in the evaluations for composite particles, which are needed for the inverse process of composite particle emission:

1. deuterons—the Lohr-Haeberli[28] and the Perey potential[29]
2. tritons—the Becchetti-Greenlees[30] potential
3. alpha particles—the McFadden-Satchler[31] potential.

Recent work in nuclear reaction theory has emphasized the importance of calculating direct inelastic scattering cross sections to low-lying states and indicated that collective direct excitations often persist into the continuum.[32] For this reason, the GNASH code has been modified to allow the inclusion of direct scattering cross sections for large numbers of states (sometimes as many as 100), including those that are embedded within the "continuum" region, where a statistical level density prescription is used, such as excitation of giant resonances. For such direct reactions, nuclear deformation parameters are obtained from the literature, and the ECIS code is used to calculate the distorted wave Born approximation (DWBA) cross sections. These are then included as input to GNASH so that the effects of their subsequent gamma-ray decay, as well as the removal of flux from other reaction mechanisms, are incorporated into the results.

Gamma-ray transmission coefficients are determined using the Kopecky-Uhl[33] formalism, which modifies the Brink-Axel hypothesis to include an excitation-energy dependence of the giant dipole (and other multipole) strength.

II.C. Level Densities

The Ignatyuk et al.[34] nuclear level densities are used, which include the washing out of shell effects with increasing excitation energy, and are matched continuously onto low-lying experimental discrete levels. The Ignatyuk model for describing the statistical level density properties of excited nuclei is particularly appropriate for the relatively high energies studied in this work. For instance, it has been shown[35] that the larger level density parameter at high excitation energies that results for nuclei near closed shells causes a lower nuclear temperature, and therefore a lower average ejectile evaporation energy, which in turn significantly influences the distribution of isotope production yields after the reaction. Our implementation of this formalism, using a constant-temperature region just above the discrete levels before the Fermi-gas region begins, also allows it to be applied at low excitation energies.

In this approach, the level density parameter is energy dependent:

$$a(U) = \alpha[1 + f(U)\delta W/U] \ , \quad (3)$$

where α is the asymptotic high-energy value. Shell effects are included in the term δW, which is determined via $\delta W = M_{exp}(Z,A) - M_{ld}(Z,A,\beta)$, where $M_{exp}(Z,A)$ is the experimental mass and $M_{ld}(Z,A,\beta)$ is the liquid-drop mass at deformation β. The exponential damping of shell effects is given by

$$f(U) = 1 - \exp(-\gamma U) \ , \quad (4)$$

where $\gamma = 0.05$ MeV. The asymptotic form of $a(U) \rightarrow \alpha$ is given by

$$\frac{\alpha}{A} = \eta + \beta A \ . \quad (5)$$

By fitting *s*-wave resonance data at the neutron separation energy, the values $\eta = 0.1375$ and $\beta = -8.36 \times 10^{-5}$ were obtained.[1]

In some cases, level density analyses were performed for all residual nuclei to determine the maximum number of discrete levels that should be used (e.g., for light nuclei such as C, N, and O, where the number of residual nucleus products is relatively small). However, since many different residual nuclei can be produced in nuclear reactions up to 150 MeV, exceeding 100 in many cases for heavy targets, in some cases we automate this procedure by always using a maximum of 10 to 15 experimental levels. This procedure is expected to be adequate for nuclear reactions induced at these relatively high incident energies—it has the merit that the nuclear levels included for each nucleus are likely to be complete up to the highest level's energy, which is important when matching a statistical level density theory onto the density of known low-lying levels.

II.D. Preequilibrium Emission

After the aforementioned steps have been completed, all input parameters are available for the GNASH calculations. An input parameter that is sometimes adjusted is the exciton model damping matrix element that governs the relative probability of emission from different steps in the preequilibrium cascade. To determine the best value to use, experimental emission spectra measurements are collected, and trial calculations are performed. The matrix element is then adjusted within the range from 140 to 175 MeV[3] (Ref. 8) to optimize the global agreement with measurements.

The semiclassical exciton model in combination with the Kalbach angular-distribution[36] systematics provides a reliable method to predict double-differential outgoing spectra for all the nuclides considered here. Since the high-energy tail of the continuum spectrum is so important—certainly for high incident energies it accounts for the major part of the reaction cross section—we have validated the exciton model's predictions through comparisons with quantum preequilibrium calculations. This approach enables a realistic prediction of angle-integrated spectra and the angular distributions without using any experiment-based phenomenology. We use the recent two-component extension[37] of the multistep direct (MSD) model of Feshbach-Kerman-Koonin.[21] It comprises a combination of DWBA matrix elements and a statistical description of the excited states of the nucleus. When a reaction proceeds by the MSD mechanism, at least one particle is in the continuum throughout the process, and at each subsequent step of the reaction, a new particle-hole pair is created. After one or a few collisions, the continuum particle is emitted in a direction that still has retained some coupling to the initial direction and is therefore forward-peaked. The main difference with conventional direct-reaction theories is the high density of final and intermediate states, which necessitates statistical postulates in the direct-reaction formalism so that the computation of these processes remains tractable. In Ref. 37 we presented a formalism for calculating MSD cross sections in a fully two-component theory, where all possible neutron and proton particle-hole excitations are explicitly followed for all orders of scattering.

Figure 4 shows comparisons of double-differential cross sections as calculated with the FKK method with experimental data[38] for the Fe(p,xn) and Pb(p,xn) reactions at 113 MeV. The good agreement obtained between the FKK predictions and experiment, and between FKK and exciton model predictions,[11] provides some confidence in the use of the exciton model in GNASH for the large-scale calculations of nuclear data described in this paper. Theoretical studies using the FKK preequilibrium theory have played another useful role in this work—a number of theoretical nuclear reaction physics developments have been made and tested within the context of the quantum multistep theory, such as multiple

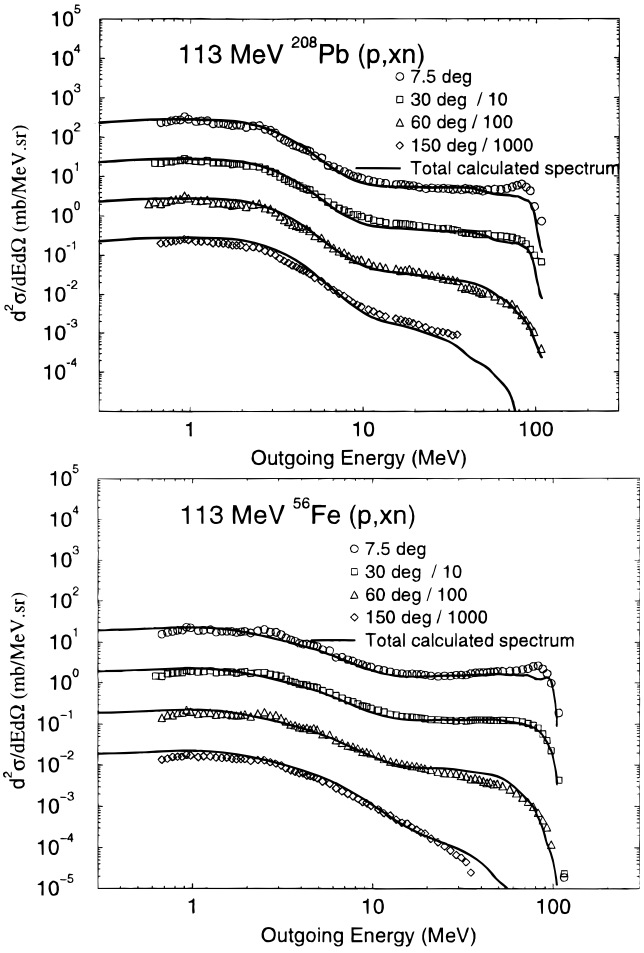

Fig. 4. Comparison of quantum mechanical FKK predictions of continuum preequilibrium emission spectra with experimental data.[38]

preequilibrium emission[12] and preequilibrium spin effects,[39] before being included in the GNASH code for nuclear data evaluation calculations.

III. CALCULATION OF RECOIL SPECTRA

The calculation of the energy spectra of secondary recoils in this work represents an advance in the completeness of high-energy ENDF files. Previous high-energy evaluation works have either omitted this information, since transport effects were the main focus of study,[1,16] or have tabulated the total energy per reaction deposited by the recoils but have neither specified recoil energy spectra nor how this energy is divided among individual recoils.[14,15] Our more complete treatment facilitates detailed calculations of radiation damage and heating. In addition, in applications that use these data in simulations of heavy-particle radiotherapy, one could utilize the recoil spectra to determine relative biological effectiveness in addition to absorbed dose because the linear energy transfer properties of the ionizing radiation are known. Clearly, kinematics determine that energy deposition by recoils (defined as all nuclides with $A > 4$) is most important for reactions on light target nuclei. Indeed, we calculate that for 20-MeV neutrons on oxygen, approximately 30% of the total energy deposition (kerma) is due to the recoils.[40]

The basic physical principles influencing recoil energies were elucidated in the 1960s by Blann and Ewart,[41] who measured recoil ranges and made use of the Lindhard-Scharff-Schiott theory for the range-energy relationship. Their findings can be briefly summarized:

1. In the formation of a compound nucleus, full momentum transfer from the projectile occurs. Compound-nucleus evaporation of a particle leads to a new recoil that has, on average, a higher kinetic energy than the kinetic energy before emission.

2. Where preequilibrium reactions occur in the first stages of the reaction, there is only a partial momentum transfer from the projectile, which results in lower kinetic energies of the first recoil nucleus after preequilibrium emission.

A more recent work by Gadioli et al.[42] also nicely demonstrates these effects.

Full details of our calculational method for recoils are described in Ref. 20. Briefly, the GSCAN code is used to read emission spectra from each decaying composite nucleus in the GNASH output. Kinematic transformations from the center of mass (c.m.) to lab reference frames are performed analytically to determine recoil lab energies, taking advantage of the simple analytic functional form of the angular distributions embodied in the Kalbach systematics.[36] Equations for these kinematic transformations are provided in the Appendix.

Since the recoiling nucleus after particle emission is frequently particle-unstable and undergoes further particle emissions, the calculation of the recoil spectra of a given product nuclide requires following the sequential particle decays in a coupled manner. The c.m.-to-lab boost velocity changes during the evolution of the reaction.[41] The initial composite nucleus lab velocity after the projectile strikes the target nucleus is rather large. However, since the first ejectile is often a preequilibrium emission with a large kinetic energy in a forward direction, the lab recoil speeds after this primary emission are reduced (which is another way of saying that only partial momentum transfer occurs). During further sequential compound nucleus decays, the recoiling nuclei tend to pick up speed again as internal excitation energy is converted to particle emission energy and recoil kinetic energy.

The resulting calculated recoil spectra are tabulated as angle-integrated spectra in the laboratory frame in the file-6 section of the ENDF evaluation. Since recoil ranges are small, a detailed representation of angle-energy-correlated recoil spectra is unnecessary for most applications. Also, the recoil spectra are represented in histogram format for ten equally sized emission energy bins. Such a coarse representation of the calculated spectra prevents the evaluated file from becoming too long, and this level of detail for the recoil information is sufficiently accurate for calculations of radiation heating and damage. We checked that the average energy of the coarsely binned recoil spectra agreed well with the exact results, which is important for ensuring that the nonelastic recoil kerma coefficients are accurately defined. Illustrative examples of recoil spectra are shown in Fig. 2.

An example of the variation in calculated recoil velocities with particle emission is shown in Fig. 5 for 80-MeV protons on ^{28}Si for processes involving sequential

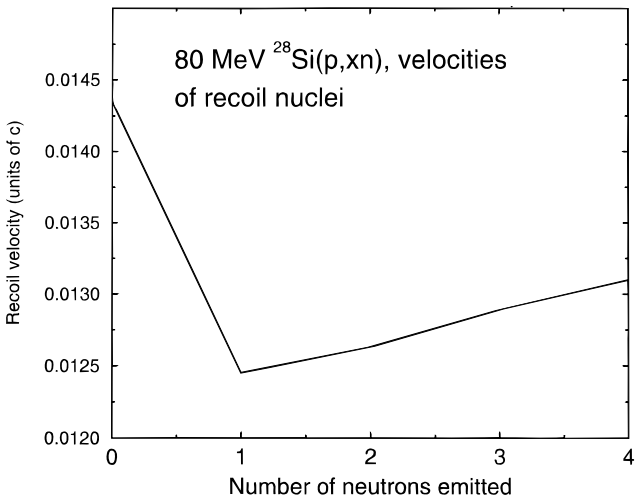

Fig. 5. Variation in average velocity of recoiling nuclei as neutrons are emitted from decaying phosphorus isotopes in the 80-MeV $p + {}^{28}$Si reaction.

neutron emission. The initial reduction in recoil velocity due to first-particle preequilibrium emission is evident, followed by increasing average recoil velocity with sequential equilibrium neutron decay.

IV. RESULTS AND COMPARISONS WITH MEASUREMENTS

IV.A. General

This section describes the evaluation methods and nuclear model calculations used for each element under study. The methods used depend on the nature of the target, and in particular, they depend on the extent to which statistical assumptions implicit in the nuclear models are valid. For this reason, the cross-section evaluations of the lightest nuclei studied here, hydrogen and deuterium, were based almost entirely on experimental data and on nuclear theory R-matrix and phase-shift representations of experimental data. The evaluations for targets such as carbon, nitrogen, and oxygen used GNASH nuclear model calculations, but they also relied heavily on measured data. Evaluations of targets heavier than oxygen were based almost exclusively on GNASH model calculations.

The comparisons in this section between the evaluated results and experimental data are critical for benchmarking the evaluations, for validation purposes, and for assessing the accuracy of the evaluated data library. Even though these comparisons are rather extensive, numerous comparison figures have been omitted due to limitations on space (which can be provided on request by the first author). The figures that we use are representative and have been chosen to emphasize nuclear reactions on targets that are most important for accelerator-driven systems, such as Pb, W, and Fe. Fewer comparisons are provided for other targets that are somewhat less important or that are documented elsewhere.[14,15,43]

IV.B. The ^{206,207,208}Pb Evaluations

The development of high-quality nuclear data for lead is particularly important due to lead's role as a spallation target and neutron multiplier in many accelerator-driven system designs.

Measurements for the total, elastic, and nonelastic cross sections for lead are shown in Figs. 6, 7, and 8, compared with our evaluated results. In the case of the total cross section, we were guided mainly by the Lisowski et al.[45] and Finlay et al.[46] data. The elastic scattering angular distributions (Fig. 7), calculated with a deformed optical potential developed for lead,[47] are seen to account for the measurements well. The total nonelastic cross section obtained from this coupled-channel calculation was modified slightly to better agree with the experimental data, as shown in Fig. 8. Figure 8 also shows the proton nonelastic cross section compared with measurements. An accurate representation of the nonelastic cross sections is important because the production cross sections of secondary ejectiles are directly proportional to this quantity (being the product of the nonelastic cross section and the ejectile yield, or multiplicity). The evaluated total and nonelastic cross sections were taken to be identical for all the lead isotopes, a good approximation due to the small relative mass differences.

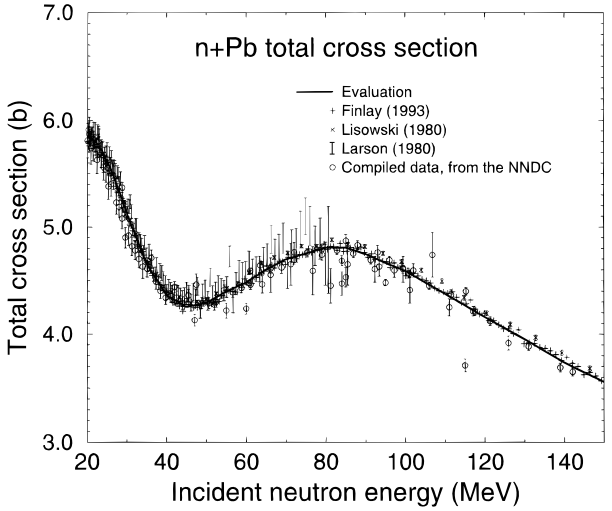

Fig. 6. Evaluated neutron total cross section for ^{208}Pb compared with measurements.

Direct inelastic scattering to low-lying levels in lead isotopes was calculated using the ECIS code, using DWBA theory. Excitation of states in the discrete level region, as well as states within the continuum region, was considered. Ninety-eight states were considered for ^{208}Pb up to an excitation energy of 7.114 MeV; 59 states were considered for ^{207}Pb up to an excitation energy of 6.483 MeV; and 13 states were considered for ^{206}Pb up to an excitation energy of 6.423 MeV. Deformation lengths for the DWBA transitions were obtained from the Nuclear Data Sheets and from Refs. 48 and 49.

The only neutron-induced emission spectra measurement above 20 MeV is that of Hjort et al.[50] for the 65-MeV Pb(n, xn) reaction at forward angles. These data are extremely useful for benchmarking the neutron-induced GNASH calculations, and Fig. 9 demonstrates that the GNASH predictions are in good agreement with these data. The fall-off in the experimental data below 20-MeV emission energy is an artifact and due to the high detector threshold energy. Some of the fluctuations seen in the measured data are due to the excitation of giant resonances high in the continuum not included in our calculations.

Numerous data for neutron production via Pb(p, xn) reactions exist. Comparisons between the evaluated results and angle-integrated emission spectra measurements at 26, 45, and 80 MeV are shown in Fig. 10. Agreement

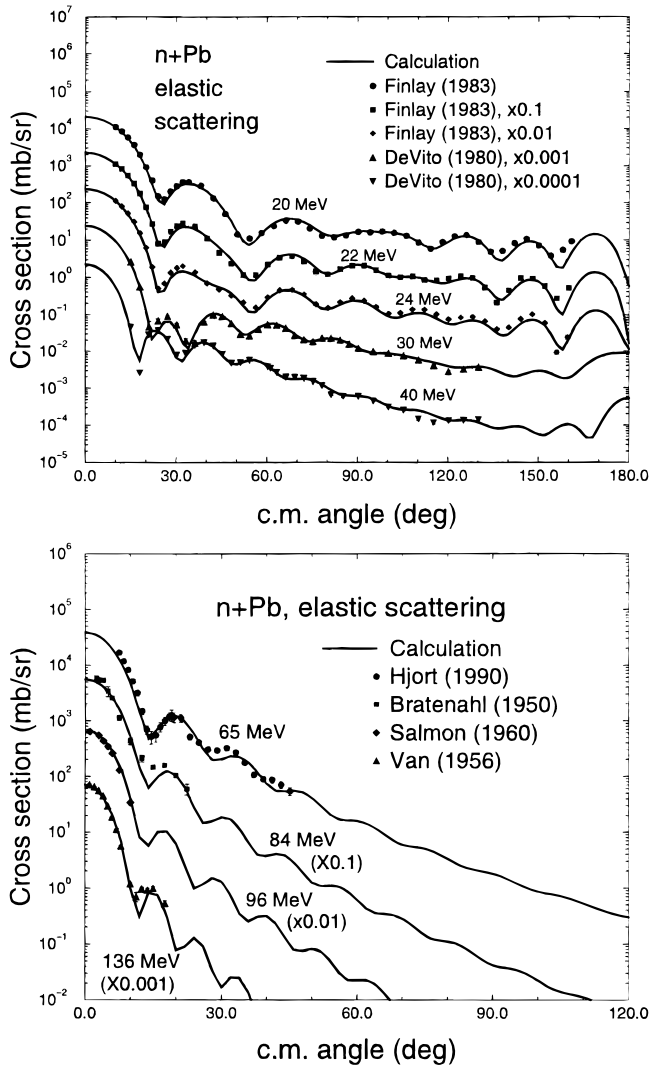

Fig. 7. Evaluated neutron elastic scattering cross section for ^{208}Pb compared with measurements.[44]

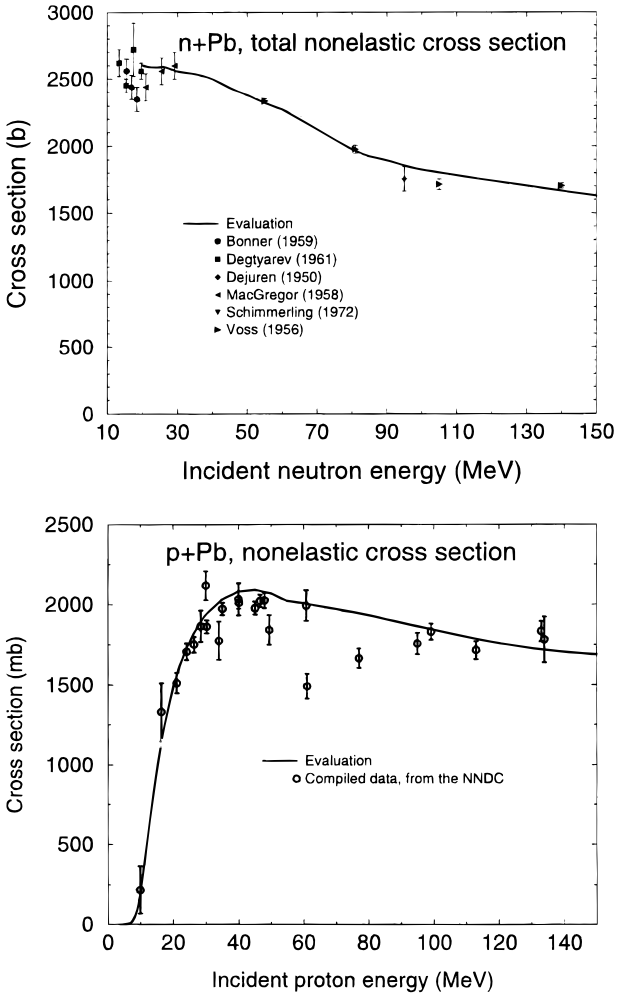

Fig. 8. Evaluated neutron and proton nonelastic cross section for ^{208}Pb compared with measurements.[44]

with the measured data is good with the exception of the 80-MeV reaction, where the calculations underpredict neutron emission in the 20- to 40-MeV energy range. At 113 MeV, the evaluation is compared to the double-differential experimental data of Meier et al.[38] in Fig. 11. Agreement is fairly good over the whole emission energy range, except at 150 deg. The magnitude of the calculated back-angle preequilibrium emission is determined by the extent of forward-backward asymmetry from the Kalbach angular-distribution systematics[36] and is therefore only as accurate as these systematics are accurate. However, the small magnitude of the back-angle cross section implies that the practical impact of the back-angle underprediction is expected to be small.

The increasing importance of preequilibrium emission with incident energy is evident in Fig. 10, as can be seen from the significant contribution of high-energy

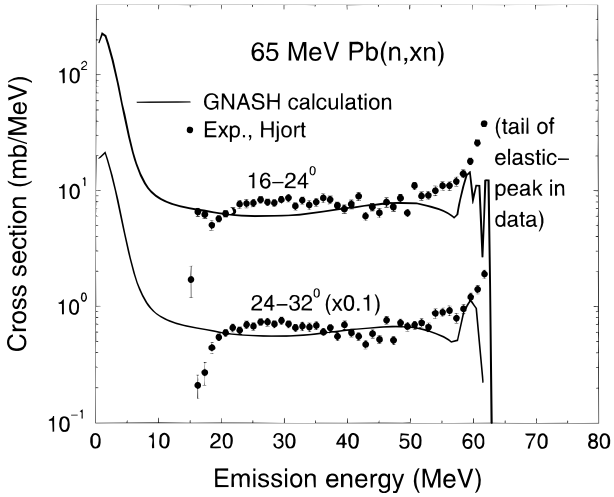

Fig. 9. Evaluated ^{208}Pb(n,xn) neutron emission spectra at 65 MeV compared with experimental data.[50]

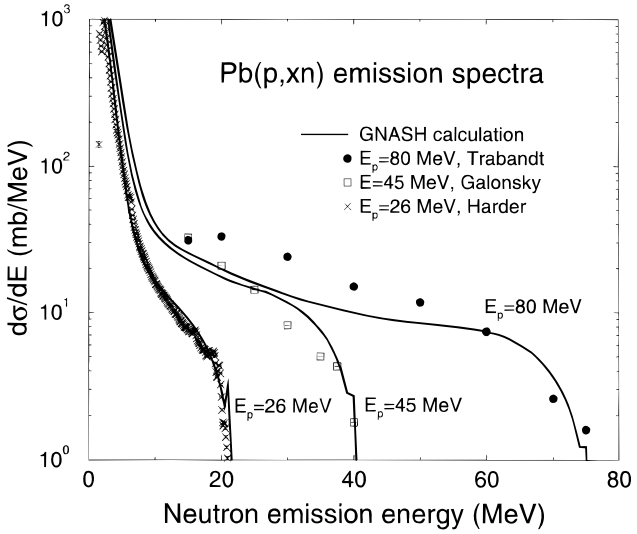

Fig. 10. Evaluated ^{208}Pb(p,xn) angle-integrated neutron emission spectra compared with experimental data[44] at incident energies of 26, 45, and 80 MeV.

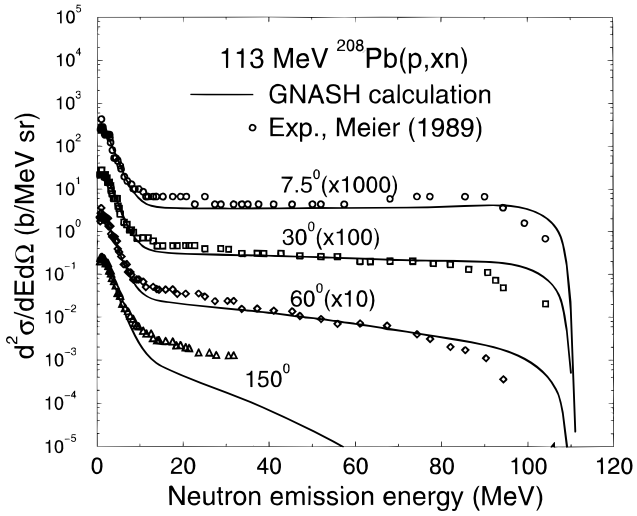

Fig. 11. Evaluated ^{208}Pb(p,xn) double-differential neutron emission spectra compared with experimental data[38] at 113-MeV incident energy.

ejectiles for the higher incident energy reactions. In addition, this figure also shows the increased neutron emission in the evaporation regime with increasing incident energy due to energy conservation (more energy is available to overcome separation energies for particle emission).

IV.C. The ^{196,198,199,200,201,202,204}Hg Evaluations

Mercury is currently receiving a great deal of interest as a spallation neutron source, particularly at accelerator facilities used in material science studies. No ENDF/B-VI evaluation exists for mercury, though recently Shibata et al.[51] have produced neutron evaluations below 20 MeV for seven mercury isotopes for the Japanese JENDL-3.3 file. Through a collaboration with these authors, we have extended their neutron evaluations up to 150 MeV using GNASH model calculations and have produced new proton evaluations from 1 to 150 MeV.

Because of the very limited number of experimental data for nucleon reactions on mercury, the evaluated data are heavily based on model calculations. An optical model originally developed by Chiba for neutron scattering on lead was adapted for use on mercury. This potential was used for the total, nonelastic, and elastic scattering distributions. For protons, the medium energy potential (Table II) was used above 20 MeV, and the Becchetti-Greenlees potential,[30] at lower energies. Deformation lengths for inelastic scattering were obtained from the analyses performed for the JENDL-3.3 evaluations.

IV.D. The ^{182,183,184,186}W Evaluations

Tungsten is a particularly important element in the APT program due to its use as the spallation neutron target. Its high melting point enables it to withstand large proton beam currents, and a high number of spallation neutrons are released per incident proton. Because low-energy neutrons have a high neutron capture cross section on tungsten, a split-target design is used to minimize neutron self-absorption.

Prior to a recent LANL total cross-section measurement,[52] only two measurements of the total cross section on tungsten existed above 20 MeV: those of Peterson, Bratenahl, and Stoering[53] and Hildebrand and Leith.[54] The new total cross-section data were taken at the Weapons Neutron Research white neutron source facility and extend from 6 to 600 MeV. Our evaluated results from 20 to 150 MeV follow these new data for elemental tungsten, which are in good agreement with the Peterson measurements (Fig. 12). Since the total cross section is expected to vary by less than ~2% among the naturally occurring tungsten isotopes, our evaluation uses the same elemental total cross section for all the isotopes.

No measurements exist for the neutron nonelastic cross section on tungsten, though there is a 90-MeV measurement of the proton nonelastic cross section by Kirby and Link.[55] Our evaluated nonelastic cross section makes use of optical model calculation results. Below 80 MeV, the neutron potential of Young and Arthur was used,[1] and above 80 MeV, the global Madland potential was used (Table II). The calculated neutron nonelastic cross section agreed well with the Kirby proton-induced measurement (after scaling by the calculated optical model ratio of neutron-to-proton nonelastic cross section at 90 MeV). The shapes of the calculated results are also consistent with measurements at other energies: data at

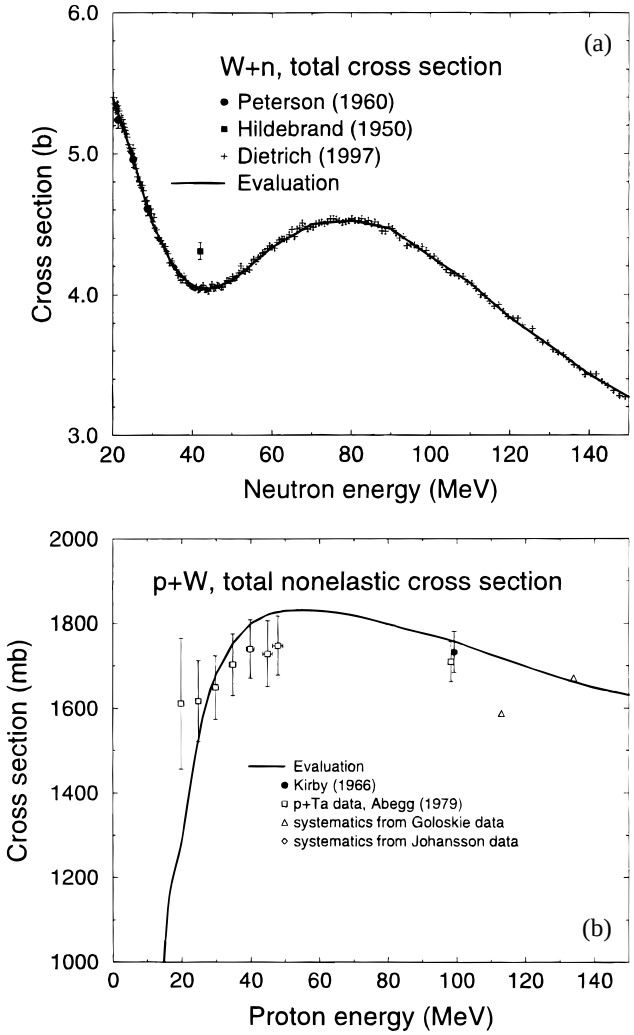

Fig. 12. Comparison of tungsten evaluation and elemental measurements for (a) total neutron cross section[44,52] and (b) proton nonelastic cross section.

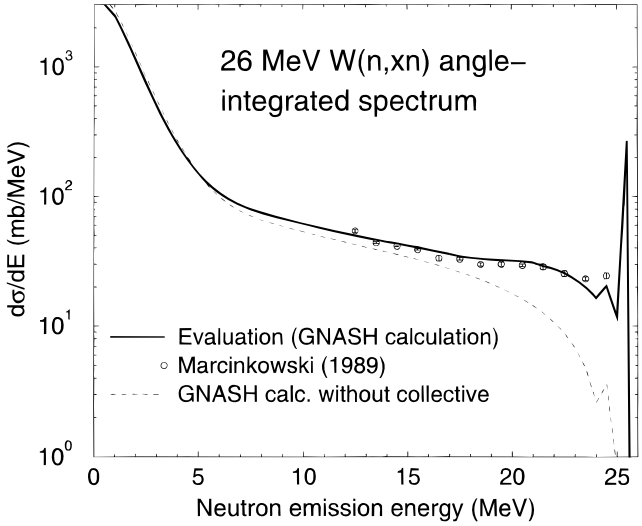

Fig. 13. Comparison of the evaluated 26-MeV $^{184}W(n,xn)$ emission spectrum with measurements.[59]

14 MeV (Ref. 56), and systematics from neutron-induced measurements on other targets at higher energies (interpolated using a mass dependence of $a + bA^{2/3}$), as shown in Ref. 57. Optical model calculations using the medium energy potential (Table II) above 20 MeV and the Becchetti-Greenlees potential at lower energies were performed for protons, with a small renormalization to better account for the measurements. The data shown in Fig. 12 include Kirby's 90-MeV value, measurements on tantalum (which would be expected to be similar since tantalum is adjacent to tungsten in the periodic table), and systematics from measurements on other targets.[44]

Direct inelastic scattering reaction mechanisms were considered for the tungsten isotopes calculated with the ECIS code. Reaction mechanisms studied included (a) excitation of low-lying rotational levels and (b) excitation of giant isoscalar 1-, 2-, and 3- (LEOR) resonances. Our calculation of these collective excitations followed that of Marcinkowski, Demetriou, and Hodgson.[58]

At 26 MeV, Marcinkowski et al.[59] have measured $^{184}W(n,xn)$ neutron emission spectra. Their angle-integrated data are compared in Fig. 13 with our calculations, and the agreement is excellent. This is due, in part, to the theoretical description of collective excitations. The GNASH calculation without collective enhancements is shown by the dashed line and substantially underpredicts the high-energy cross sections. The excitation of the giant isoscalar broad resonances account for the cross section given by the difference between the solid and dashed lines in Fig. 13; the calculated peak at the highest emission energies is due to the excitation of rotational levels. The agreement seen in Fig. 13 is significantly better that that found in the model calculations contributed to the 1988 Code Intercomparison[60] because of the inclusion of continuum collective effects in this work.

A measurement of neutron production in the 113-MeV proton-induced reaction on tungsten was made by Meier et al.[38] (see Fig. 14). The only other existing measurement for neutron production is from Skyrme.[61] A number of factors, however, suggest that the double-differential Meier et al. data may be ~50% too high:

1. Skyrme's data[61] for tungsten are significantly lower and in good agreement with our evaluation (Fig. 15).

2. Comparisons with other Meier data, such as data for a lead target,[38] indicate that the tungsten data appear to be anomalously high for all emission energies and angles.

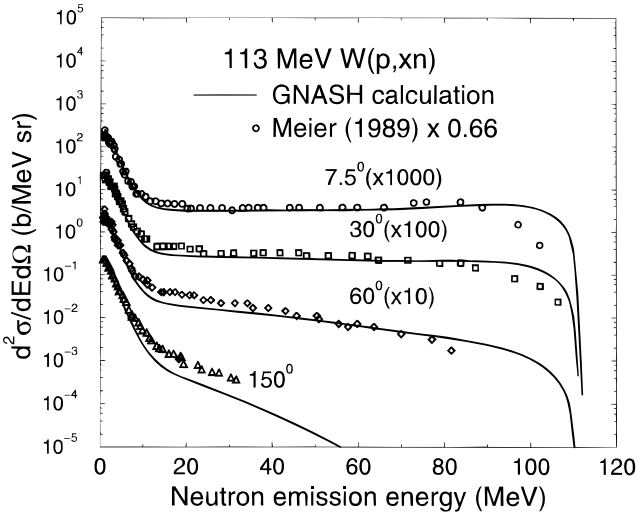

Fig. 14. Evaluated W(p,xn) double-differential neutron emission spectra compared with experimental data[38] at 113-MeV incident energy. The measurements have been decreased by a factor of 0.66 (see text).

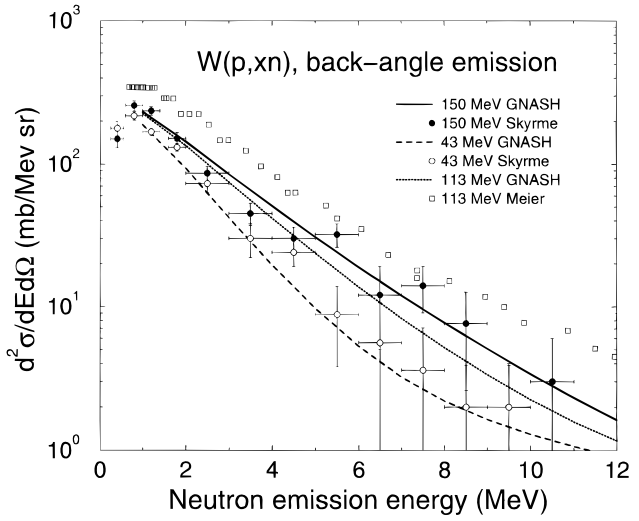

Fig. 15. Comparisons between calculated W(p,xn) back-angle emission spectra in the evaporation regime with measurements by Meier et al.[38] and Skyrme.[61] The calculations are consistent with the Skyrme data but not the Meier et al. data.

3. Energy balance arguments argue against the high neutron emission multiplicity implicit within the Meier et al. data.

These factors are discussed in detail in Ref. 62. Figure 14 shows our calculated emission spectra at four angles, and when the Meier et al. measurements are scaled by a factor of 2/3, the agreement is seen to be good. The calculated neutron production spectra in the low-emission-energy evaporation region are compared with Skyrme's measurements at 42 and 150 MeV in Fig. 15. Again, the Meier et al. data appear to be inconsistent with both our calculations and the Skyrme data.

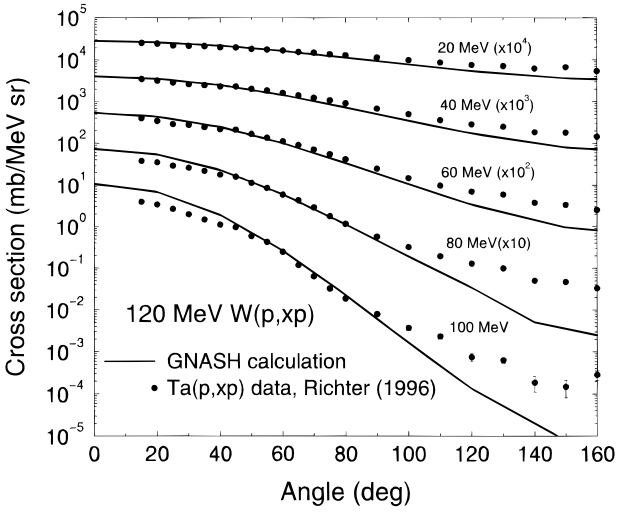

Fig. 16. Comparison between calculated 120-MeV W(p,xp) angular distributions with experimental data for the 120-MeV Ta(p,xp) reaction.

No W(p,xp) measurements exist, but Richter et al.[63] have recently measured Ta(p,xp) emission spectra at 120 MeV at the National Accelerator Center in Faure, South Africa. These data are useful for benchmarking our calculations because continuum emission spectra for tungsten and tantalum would be expected to be similar at this energy. Figure 16 shows calculated angular distributions at various emission energies compared with these data. The increase in forward peaking with increasing emission energy is evident, and the calculations using Kalbach angular-distribution systematics[36] are seen to describe the variations in the data with angle over many orders of magnitude. At the highest emission energy (100 MeV), our calculations overpredict the measured proton emission at the forward angles.

IV.E. The ^{93}Nb Evaluation

Niobium is present at the 5.5% level, by weight, in Inconel-718.[a] This is a structural alloy used in the LANL APT design in the proton beam window. It is also used for structural support of the tungsten spallation neutron target tubes and for cladding the tungsten tubes to prevent water corrosion. Furthermore, niobium is present in the superconducting cavities in the proton accelerator, and nuclear reactions on niobium must be understood to simulate accidental beam-spill scenarios.

Global optical potentials described in Sec. II.B, including the medium energy potential in Table II, were

[a]Inconel is a trademark of the Inco family of companies.

used. The total cross-section evaluation was based on Finlay et al.'s[46] data. The evaluation of secondary production cross sections was based on GNASH nuclear model calculations, along with ECIS calculations describing the direct excitation of vibrational states (excitation of $2+$ and $3-$ phonon states coupled to the $4.5+$ core). Our results are compared in Fig. 17 with experimental 26-MeV Nb(n,xn) angle-integrated data[64] and with double-differential 65-MeV Nb(p,xp) data.[65] Good agreement is observed. The 26-MeV neutron scattering data were analyzed by many researchers for an international code intercomparison, organized by Gruppelaar and Nagel[66]—the level of agreement between calculation and measurement evident in Fig. 17 is an improvement on the calculations performed for this intercomparison, primarily because of our inclusion of collective excitations at the highest emission energies. Our evaluation is also consistent with new (p,xp) data at 14 MeV obtained by Watanabe.[67]

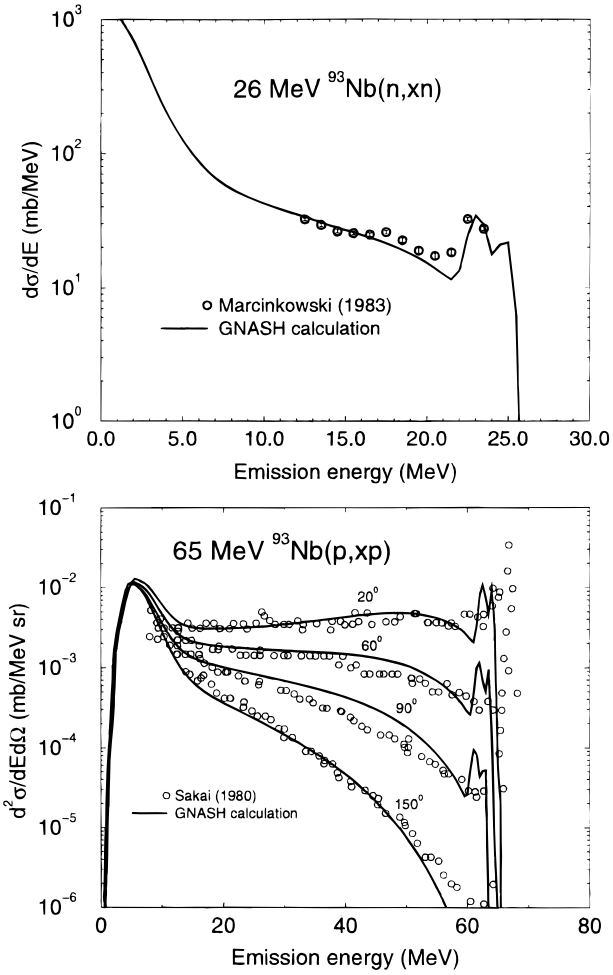

Fig. 17. Comparison between calculated and measured emission spectra for niobium.

IV.F. The ^{63,65}Cu Evaluations

The neutron total cross section above 20 MeV was obtained by evaluating experimental data, with a particular emphasis on the Finlay elemental data.[46] This resulted in an evaluated elemental Cu total cross section; to obtain isotopic ^{63,65}Cu total cross sections, it was assumed that ^{63}Cu and ^{65}Cu have total cross sections in an $A^{2/3}$ ratio to one another. The total neutron nonelastic cross section was obtained directly from an optical model calculation after verifying that it was in good agreement with the experimental data.

A neutron optical potential with a functional form described by Eq. (1) was obtained by a least-squares parameter search to fit experimental total cross-section data[46] and elastic scattering distributions from 1.6 to 96 MeV (Ref. 44). This optical potential was used for ECIS calculations of neutron transmission coefficients and DWBA cross sections for the entire energy region above 20 MeV.

Due to the lack of proton elastic scattering data in numerical form, we used a combination of global optical models for the proton channel. The Becchetti-Greenlees potential[30] was adopted below 47 MeV, and the nonrelativistic version of the Madland potential (Table II), above 47 MeV. At this particular energy, the two potentials join smoothly. Following Delaroche et al.,[67,68] we adopted the weak-coupling model for direct collective inelastic scattering for ^{63,65}Cu, using even-even ^{62,64}Ni cores, respectively. For the calculation of the cross sections, ECIS was used in DWBA mode. Deformation lengths were obtained from the literature.

The copper isotope evaluations are documented in detail in Ref. 69; therefore, further details are not repeated here. Reference 69 provides numerous comparisons against experimental total, reaction, elastic, and emission spectra data to benchmark the evaluations.

IV.G. The ^{58,60,61,62,64}Ni and ^{50,52,53,54}Cr Evaluations

Nickel and chromium are important structural elements in steel. A significant number of experimental data exist to benchmark our 150-MeV evaluations, particularly for Ni, where proton-induced emission spectra are available at 60-, 90-, 120-, and 150-MeV incident energies, and neutron-induced alpha production data exist up to ~50 MeV. The methods used to evaluate the chromium isotope cross sections followed closely those used for nickel and are therefore not described in this paper. Furthermore, apart from total, total nonelastic, and elastic scattering data, few measurements exist for Cr.

The Ni neutron total cross sections were evaluated based on the least-squares method, taking into account the experimental data,[44] including the recent elemental Ni results from LANL by Dietrich et al.[52] The total cross-section data for natural Ni were transformed to those for Ni isotope cross-sections according to an $A^{2/3}$ dependence.

The evaluated total cross-section data, *s*-wave strength functions,[25] and elastic scattering angular distribution data[44] were used to obtain the neutron optical potential parameters, with a potential functional form given by Eqs. (1) and (2). The parameter estimation was carried out based on the Marquart-Bayesian approach, where the ECIS code was used for the optical model calculations. The initial potential parameters were taken from Koning, Delaroche, and Bersillon.[70] This potential was used for the calculation of neutron transmission coefficients and DWBA cross sections in the entire energy region above 20 MeV. Below 20 MeV, the Harper neutron potential[71] was used. For protons, above 50 MeV we obtained a potential after performing a parameter search on experimental elastic and nonelastic data. Between 5 and 50 MeV, the results from Ref. 70 were used, and below 5 MeV, the Harper potential was used.[71] For deuterons, the Lohr-Haeberli[28] global potential was used; for alpha particles the McFadden-Satchler potential[31] was used; and for tritons the Becchetti-Greenlees[30] potential was used.

Direct collective inelastic scattering to levels in the Ni isotopes was calculated using the DWBA mode in ECIS. The deformation lengths were taken from Nuclear Data Sheets or from Ref. 70. However, for ^{60}Ni we just included inelastic scattering to the $2+$ vibrational state, with a deformation length that resulted in a match with the ENDF/B-VI inelastic scattering at 20 MeV because the use of deformation parameters given in Ref. 70 appeared to overestimate the magnitude of inelastic scattering.

Above 20 MeV, new measurements from Haight et al.[72] exist for alpha production on the Ni isotopes. Because alpha emission represents a small fraction of the total reaction cross section, its prediction by a nuclear model calculation is sensitive to the level density and optical potential parameters used. This fact allows such data to be used to infer level densities in the residual nucleus following alpha emission and in the residual nucleus following neutron emission, the dominant competition channel.[72] Our results, which include a fine-tuning of level density parameters to match both measured *s*-wave resonance spacings and $(n, x\alpha)$ data, are shown in Fig. 18. This provides a good example of the important role that experimental data can play in guiding a model calculation for an evaluation. If default parameters were used, it is likely that these alpha-production data would not be well predicted.

Other measurements exist for proton-induced reactions, primarily for the ^{58}Ni target. At 90 MeV, our calculations of proton, neutron, deuteron, and alpha emission agree well with measured data from the University of Maryland,[73,74] as shown in Fig. 19. At the highest emission energies, preequilibrium alpha emission is overpredicted; however, cross sections for preequilibrium cluster emission are difficult to predict accurately, and even though the data are overpredicted, their magnitude is very small, so the impact of this on applications such as energy deposition is small. Where the alpha cross section is high, at low emission energies, the calculated cross section from compound nucleus decay agrees with the measured data. At 65 MeV, our results are in excellent agreement with the proton emission spectra of Sakai et al.[65] Finally, continuum proton emission spectra have been measured[75] at the National Accelerator Center at Faure, South Africa, at 100-, 120-, and 150-MeV incident energies. Our results, shown in Fig. 20, are in excellent agreement with these data.

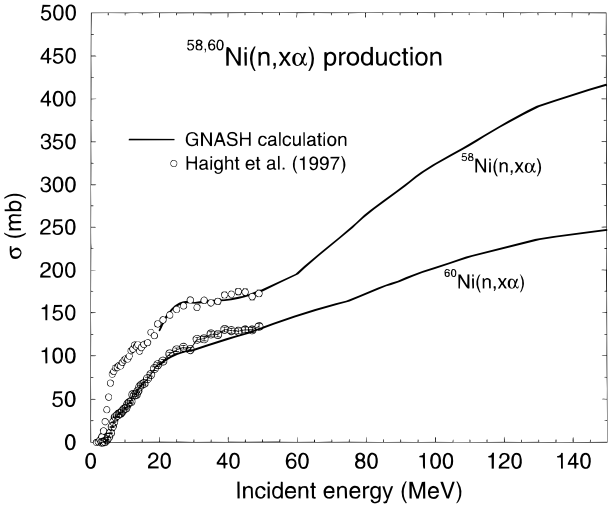

Fig. 18. Comparison between calculated and measured[72] alpha-particle production from Ni isotopes.

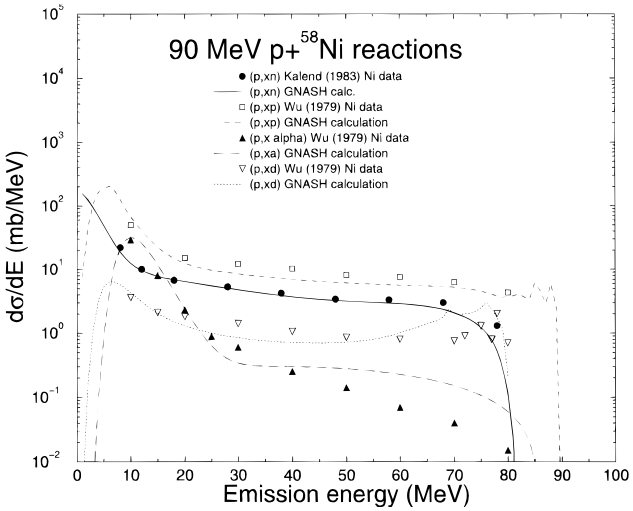

Fig. 19. Comparison between calculated and measured[73,74] angle-integrated emission of neutrons, protons, deuterons, and alpha particles for 90-MeV protons on ^{58}Ni.

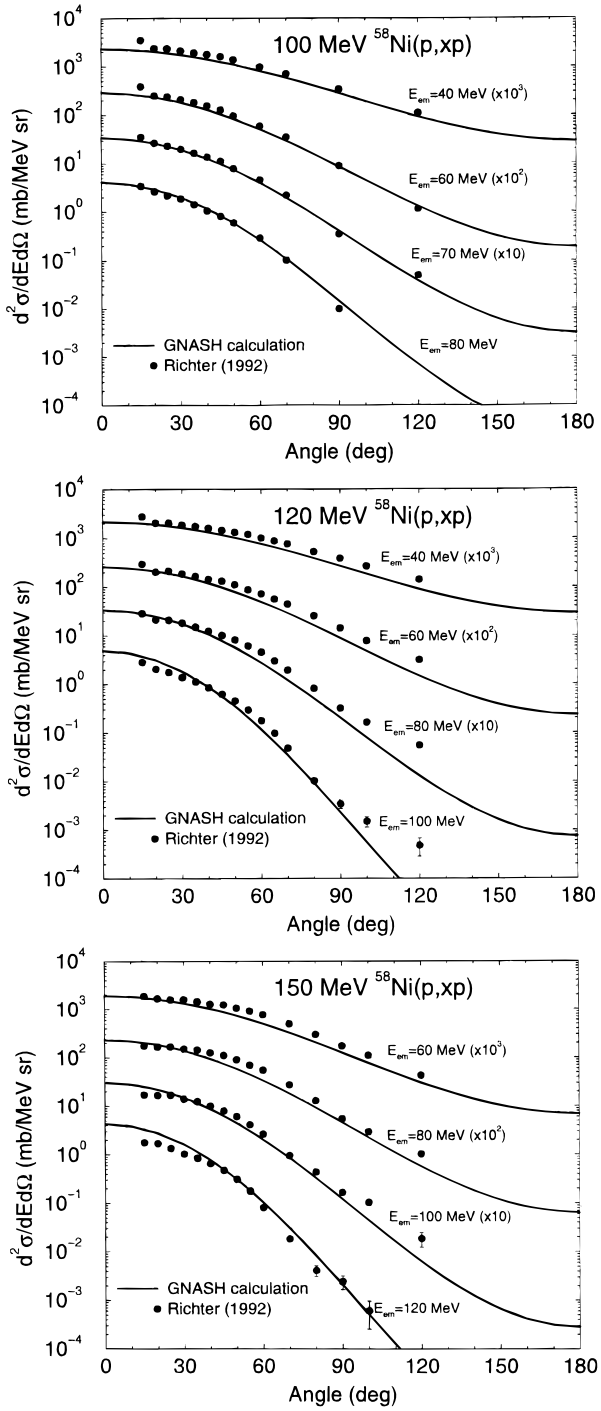

Fig. 20. Comparison between calculated and measured[75] secondary proton angular distributions for 100-, 120-, and 150-MeV protons incident on ^{58}Ni.

IV.H. The ^{54,56,57}Fe Evaluations

Because of the abundance of iron in target/blanket designs, the 150-MeV neutron and proton evaluations are discussed in some detail in this section.

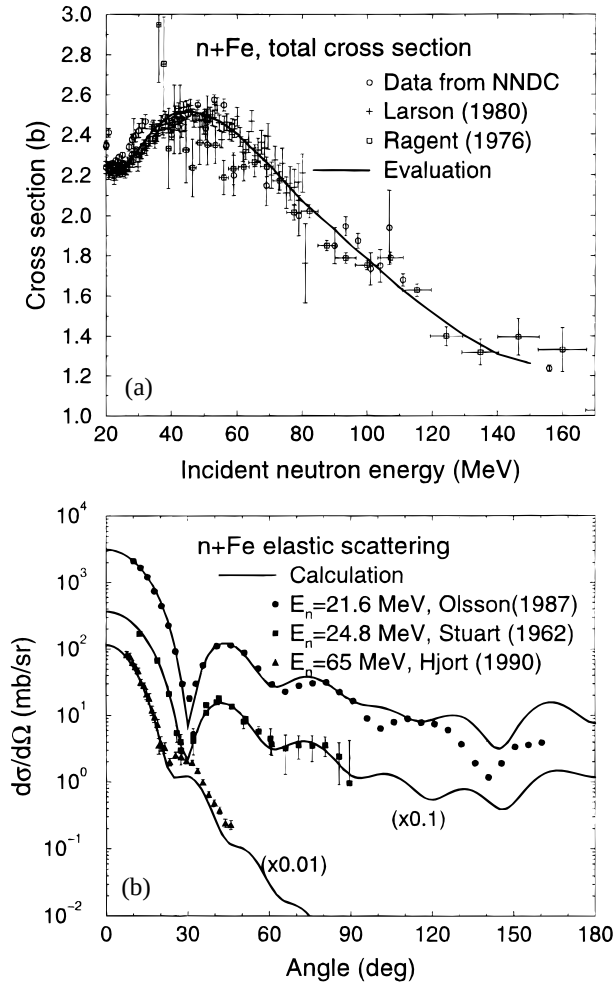

Fig. 21. Comparison of iron evaluation and elemental measurements for (a) total neutron cross section[44,52] and (b) neutron elastic scattering cross sections.

Figure 21 shows the evaluated neutron total cross section compared with data. Below 40 MeV, we have placed a particular emphasis on the Larson Oak Ridge National Laboratory measurements rather than the higher values measured by Cierjacks.[44] Elastic scattering angular distributions for neutrons are also shown in Fig. 21, calculated from the Arthur-Young optical potential[76] below 50 MeV and the medium energy potential (Table II) at higher energies. Agreement is good, except that the calculations underpredict the scattering data beyond the first minimum for the 65-MeV data. This failing is due to our use of a global potential at this energy, rather than a potential that has been fitted to the iron elastic scattering data. However, the practical impact of this underprediction is likely to be small because the cross section is low here, and where the cross section is large (at small angles), the agreement with experiment is good.

The total nonelastic cross section is shown in Fig. 22 for incident neutrons and protons. Only three neutron

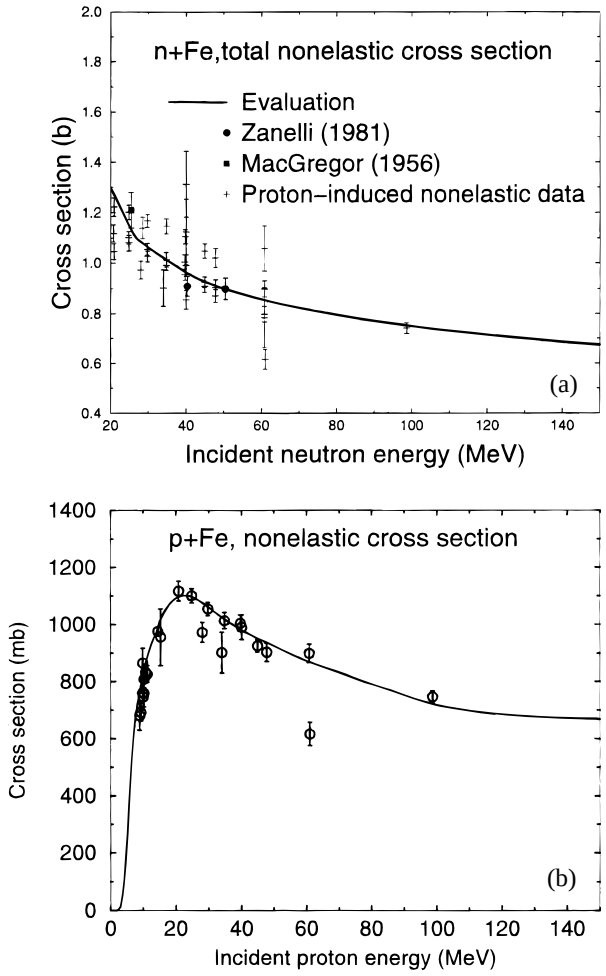

Fig. 22. The evaluated neutron and proton nonelastic cross section for Fe compared with measurements.[44]

measurements exist between 20 and 150 MeV; therefore, we also show existing proton nonelastic cross-section data in Fig. 22a for incident neutrons. (We expect the proton and neutron nonelastic data to be comparable at energies well in excess of the Coulomb barrier.) The calculated neutron nonelastic cross section from the optical model was slightly modified above 50 MeV to smooth the transition between the two potentials used. The total proton nonelastic cross-section evaluation is also compared with experimental data in Fig. 22, obtained from the compilation by Carlson.[77]

Two measurements of neutron-induced neutron emission spectra exist above 20 MeV: The 26-MeV Marcinkowski et al.[64] measurement at Ohio University and the recent 65-MeV (n,xn) measurement at forward angles by Hjort et al.[50] at the University of California-Davis. From Fig. 23 it is evident that our calculations describe the 26-MeV angle-integrated data well, including the collective excitations at higher energies (some discrepancies between experiment and theory exist in the 20- to 23-MeV region, but the calculations do reproduce the general features of the experimental data). This is due to our DWBA direct reaction calculations of transitions to all states where deformation-parameter information exists. We also include the fragmented low-energy-octopole-resonance state, which accounts for the broad peak at 17.5 MeV in Fig. 23a. Our calculations also agree well with the 65-MeV double-differential measurements of Hjort et al., where we applied Kalbach angular distribution systematics and converted the results into the laboratory frame of reference.

Secondary particle emission spectra following proton-induced reactions are shown in Fig. 24. The upper graph shows the calculated 113-MeV Fe(p,xn) differential spectra at four angles, compared with the Meier et al. data.[38] Agreement is seen to be reasonable, even at the backward angle. However, the calculations overpredict neutron emission in the evaporation regime. At 60 MeV

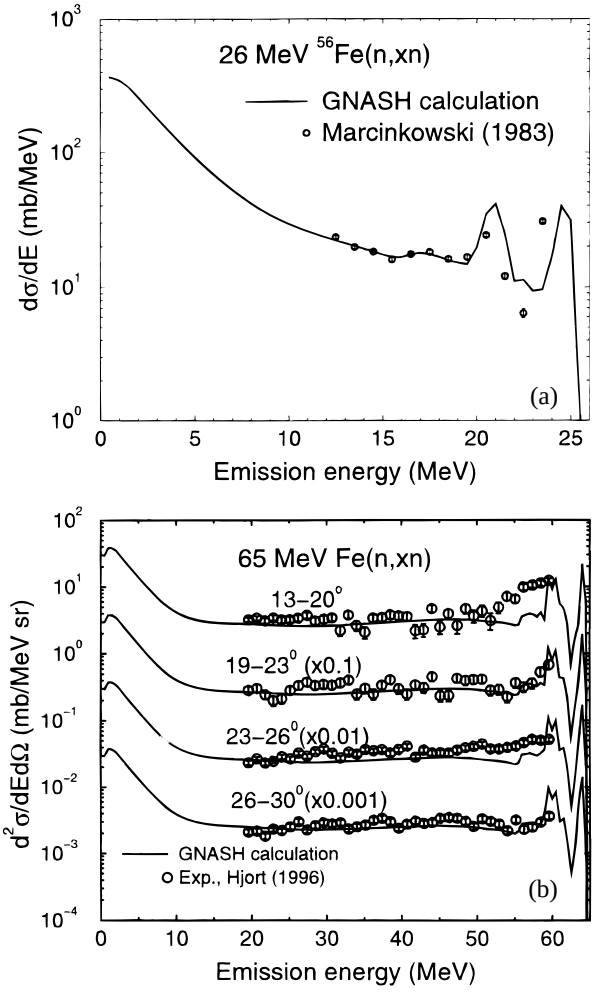

Fig. 23. Comparison of evaluated ^{56}Fe(n,xn) emission spectra with measurements: (a) 26-MeV angle-integrated data[64] and (b) 65-MeV double-differential data.[50]

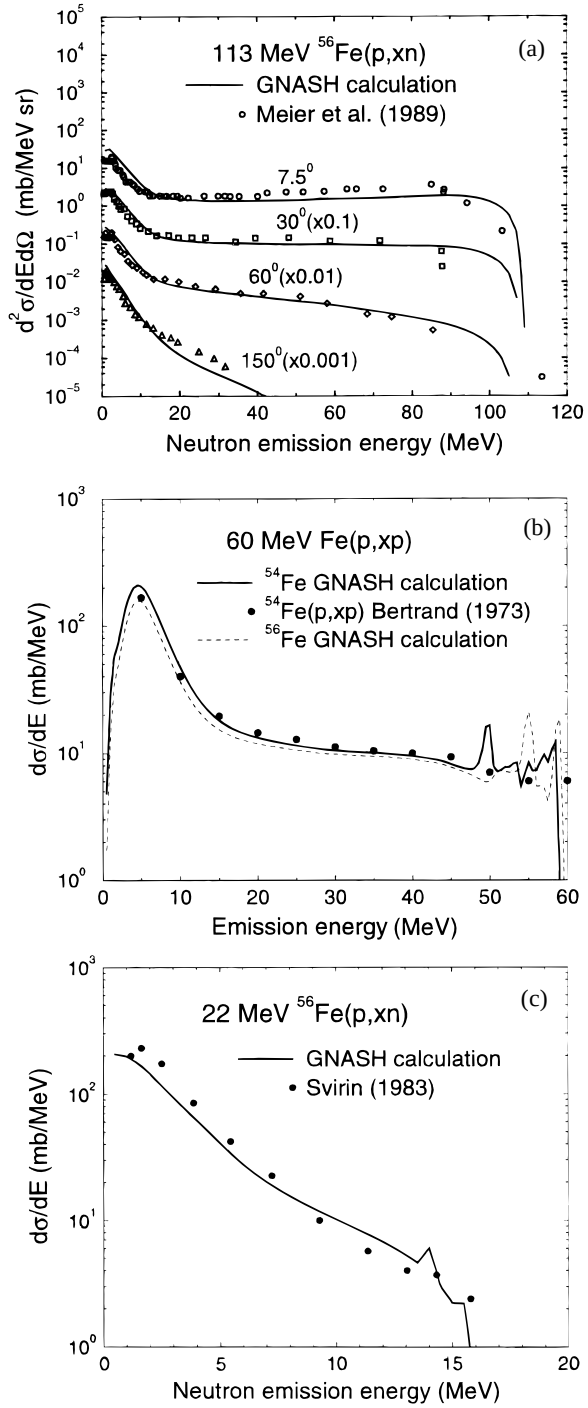

Fig. 24. Comparison of evaluated p + Fe emission spectra with measurements: (a) 113-MeV (p, xn) double-differential emission spectra,[38] (b) 60-MeV (p, xp) angle-integrated spectra,[78] and (c) 22-MeV (p, xn) angle-integrated emission spectra.[44]

(Fig. 24b), (p, xp) experimental[78] and calculated angle-integrated spectra are shown for ^{54}Fe, and again the agreement is seen to be good. For comparison, results for the emission spectra for ^{56}Fe are also shown—the differences in magnitude of proton compound nucleus emission evident in the figure are mainly due to the different Q values for the two isotopes. (Different Q values means that after particle emission, the respective residual nuclei are populated at different levels of excitation energy, where the level density is very different.) Figure 24c shows the angle-integrated Svirin 22.4-MeV ^{56}Fe(p, xn) data.[44] The calculations underpredict the measured low-energy neutron production by ~20%.

In 1997, Watanabe et al. presented (p, xp) spectra for iron isotopes at 14 and 26 MeV at the International Conference on Nuclear Data for Science and Technology, in Trieste, Italy.[79] Our calculated results, obtained prior to the measurement, are in good agreement with these data.

As discussed earlier, the evaluated cross-section libraries include results for isotope production to facilitate studies of activation, energy deposition, and radiation damage. As an illustrative example of the information included in the files, Fig. 25 shows evaluated isotope production cross sections compared with experimental data for incident protons. The same axis scales are used for all the curves shown, and the results are ordered according to decreasing magnitudes of maximum production cross section. The calculated excitation functions are seen to agree with the measured data best where the production cross sections are large (at the ~20% level), but the discrepancies become larger for the small cross sections (a factor of 5 to 10 for cross sections below 1 mb). These results are comparable to the best results shown in the recent international code comparison on intermediate energy activation yields.[81]

IV.I. The ^{28,29,30}Si Evaluations

The neutron total cross section above 20 MeV was obtained by evaluating the experimental data[44,46] (see Fig. 26). Since ^{28}Si comprises 92% of elemental silicon, the ^{28}Si total cross section was obtained by evaluating the elemental data. Total cross sections for ^{29,30}Si isotopes were obtained from the ^{28}Si evaluation after scaling the values by an $A^{2/3}$ dependence.

The global medium-energy optical potential in Table II was used for neutrons above 46 MeV, and the Wilmore-Hodgson potential was used for lower neutron energies. The global medium-energy optical potential was used for protons above 28 MeV, and the Becchetti-Greenlees potential was used for lower proton energies. In both cases the transition region to the medium-energy potential was chosen to give approximate continuity in the reaction cross section. While the aforementioned optical potentials did describe the experimental proton nonelastic cross-section data fairly well, we modified the theoretical predictions slightly to better agree with the measurements and renormalized the transmission coefficients accordingly. In addition to using Si nonelastic proton cross-section measurements, we also were guided by p + Al nonelastic data scaled by $A^{2/3}$.

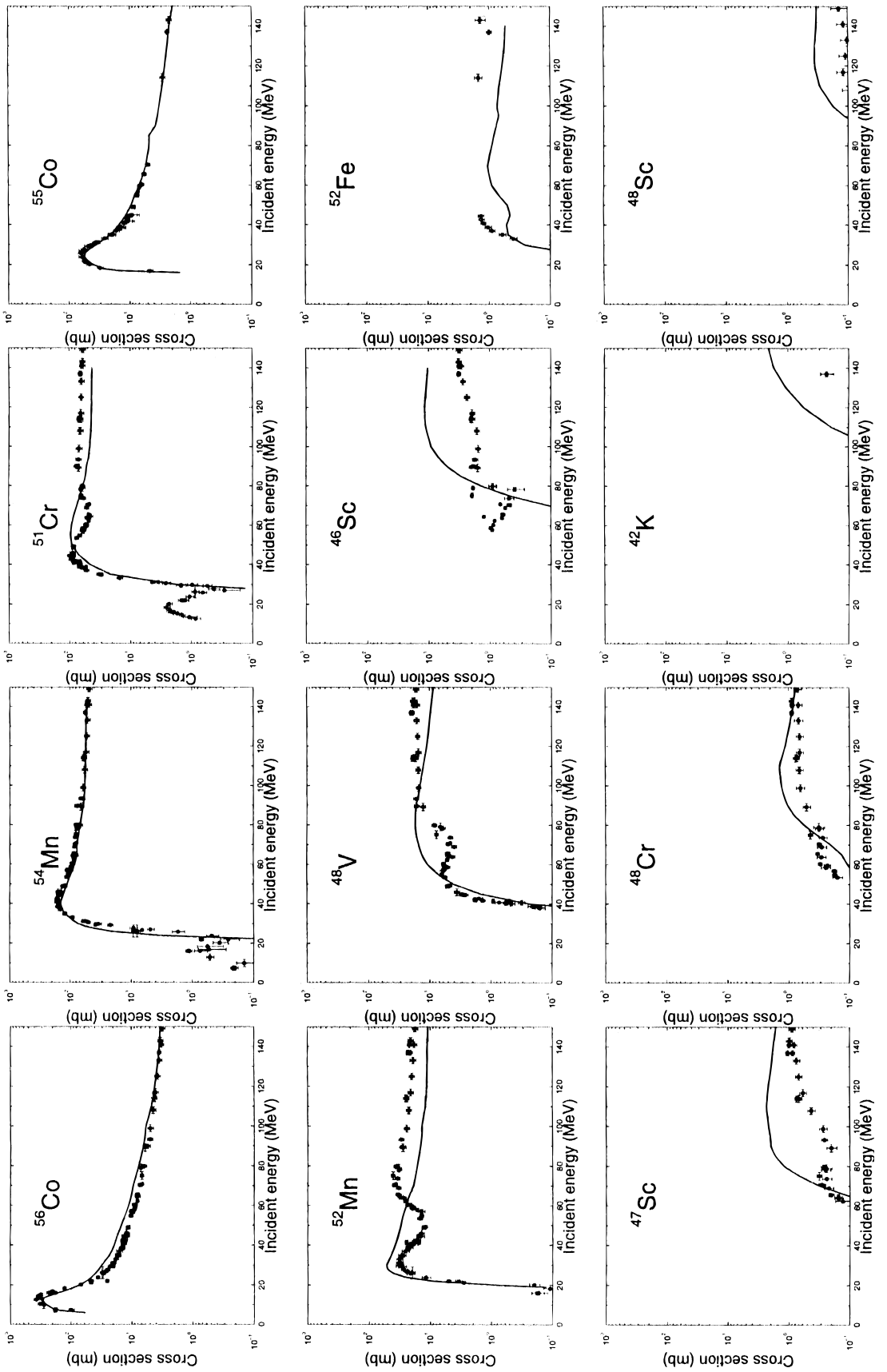

Fig. 25. Comparison of evaluated p + Fe radionuclide production cross sections with experimental data.[80]

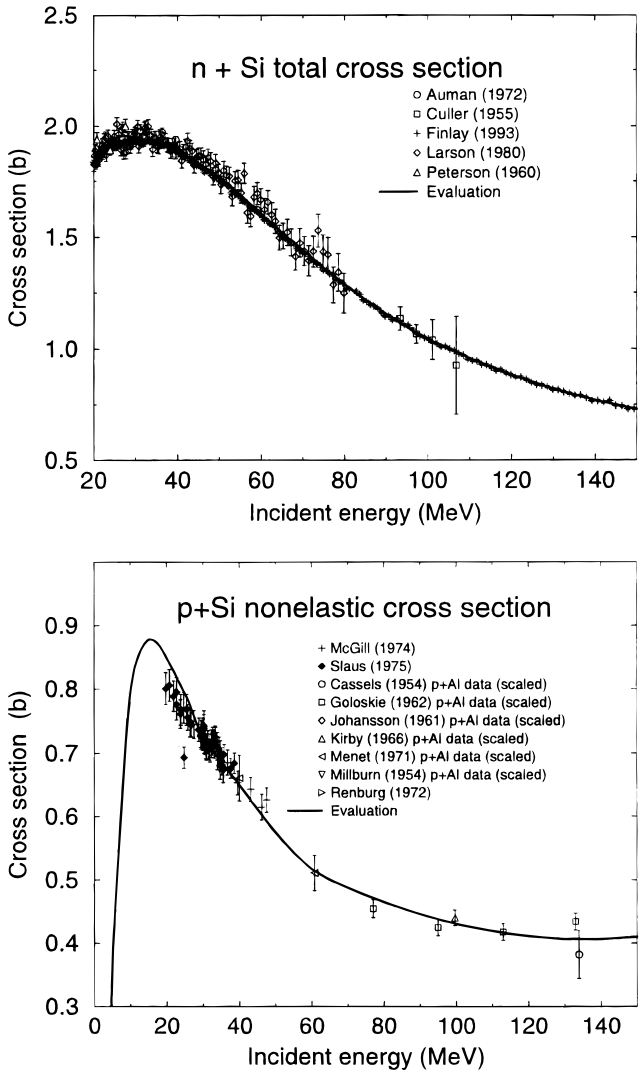

Fig. 26. Comparison between evaluated neutron total cross section and proton nonelastic cross section for silicon compared with measurements.[44,77]

Coupled-channel optical model calculations were performed to determine inelastic scattering on ^{28}Si for the $0+$, $2+$, and $4+$ states as well as a DWBA calculation of the inelastic scattering to the $3-$ vibrational state, all performed with the ECIS code. To produce continuity in the calculated inelastic cross sections up to 150 MeV, we performed a rotational band ($0+$, $2+$, $4+$) coupled-channel calculation using the global medium-energy potential in Table II (with its imaginary potential reduced by 20%, to approximately account for the coupling) over the whole neutron energy range. Deformation parameters were chosen to reproduce the ENDF/B-VI cross sections at 20 MeV, resulting in values of $\beta_2 = -0.365$ and $\beta_4 = +0.22$, in reasonable agreement with Alarcon and Rapaport's values of -0.37 and 0.17, respectively.[82] A vibrational DWBA calculation was performed for the $3-$ state resulting in $\beta_3 = 0.235$ (Alarcon and Rapaport obtained 0.23) (Ref. 8). These same β values were used for the proton inelastic scattering calculations. For ^{30}Si, inelastic scattering to the $2+$ (2.24 MeV) and $4+$ (5.95 MeV) states was also determined using a coupled-channel ECIS calculation. Deformation parameters were chosen to reproduce the JENDL-3 evaluation at 20 MeV (Ref. 83). The resulting deformation parameters ($\beta_2 = -0.33$ and $\beta_4 = 0.20$) were close to those used for ^{28}Si. Due to the small natural abundance of ^{29}Si, a coupled-channel calculation was not performed. Instead, the JENDL-3 evaluated results for inelastic scattering to the $5/2+$ (2.03-MeV) and $3/2+$ (2.43-MeV) states at 20 MeV were extrapolated to higher energies using an inverse-incident energy variation.[84]

Only two measurements exist for neutron-induced emission spectra above 20 MeV for Si. New data have been published by the Louvain group for 63-MeV Si(n,xz) double-differential spectra ($z = p,d,\alpha$ ejectiles).[85] Our calculations agree reasonably well with these measurements (Fig. 27). The angle-integrated data were obtained by performing an angle integration of the results presented by Lambert et al. in Ref. 85. In addition, Bateman et al. have preliminary data for Si(n,xp), for neutrons up to 50 MeV, including emission spectra at four angles, which are compared to our calculations in Ref. 86. While default level density parameters (using the Ignatyuk model) were utilized, in the case of ^{28}Al the level density parameter was slightly modified to optimize agreement with the Abfalterer et al.[87] total level density measurements based on fluctuation analyses.

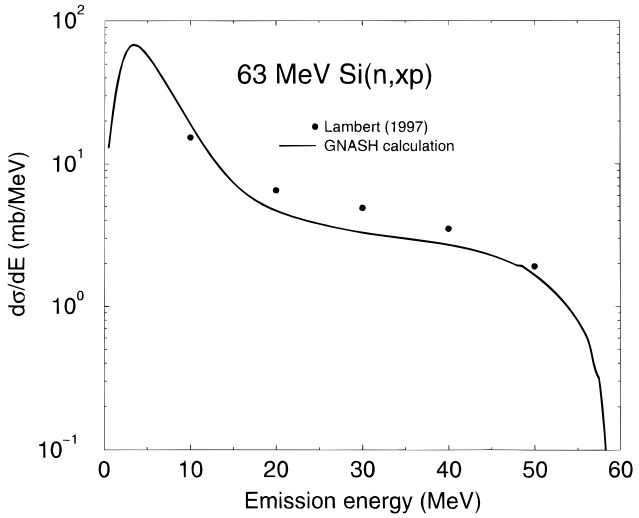

Fig. 27. Comparison between evaluated angle-integrated 63-MeV Si(n,xp) spectra with measurements.[85]

IV.J. The ^{27}Al Evaluation

The neutron total cross section was evaluated from available experimental data. From 20 to 40 MeV, the existing ENDF/B-VI (release 5) total cross-section evaluation of Young et al.[56] was adopted; from 40 to 150 MeV, the evaluation was based primarily on Finlay's 1993 measurements.[46] Figure 28 shows our evaluation compared with the experimental data.

The optical potential of Petler et al.,[88] specially developed for n + Al elastic scattering, was used for neutrons up to 60 MeV, and above this energy, the medium-energy potential was used (Table II). For incident protons, the Petler neutron potential was modified to account for proton scattering up to 60 MeV using a Lane transformation, and again the medium-energy potential was used at higher energies. The DWBA calculations were performed for inelastic scattering to low-lying states. Figure 28 also shows our evaluated neutron and proton nonelastic cross sections compared with experimental data. For incident neutrons, the figure illustrates the predictions obtained from optical model analyses and how these predictions were modified, on the basis of measured data, to obtain an evaluated nonelastic cross section. The evaluated neutron elastic scattering distributions are shown in Fig. 29 in a comparison with experimental data.

A measurement of the emission spectra for p, d, t, and α ejectiles in the 63 MeV n + Al reaction has recently been performed by Benck et al.[89] at Louvain-la-Neuve. These data are important because few such measurements exist for neutrons above 20 MeV. Detailed comparisons between our evaluated cross sections and the measurements are presented in Ref. 89 and are, therefore, not repeated here. In addition, our evaluated neutron-induced cross sections on aluminum are compared to discrete gamma-ray cross-section measurements from decaying product nuclei in Ref. 90.

The evaluated double-differential emission spectra, after conversion into the laboratory frame of reference, are compared in Fig. 30 with experimental measurements at 90 MeV and 113 MeV (Refs. 38, 73, and 74). The 90-MeV measurements from the University of Maryland are of particular interest because they are for both emitted protons and neutrons and, therefore, present a stringent test of the model calculations. Agreement with the GNASH calculations is seen to be reasonable, except for proton emission at the most forward angles and for particle emission near 20 MeV just above the evaporation peak. In particular, the calculations agree with the experimental results, showing an approximate ratio of pre-equilibrium proton-to-neutron emission of 2:1.

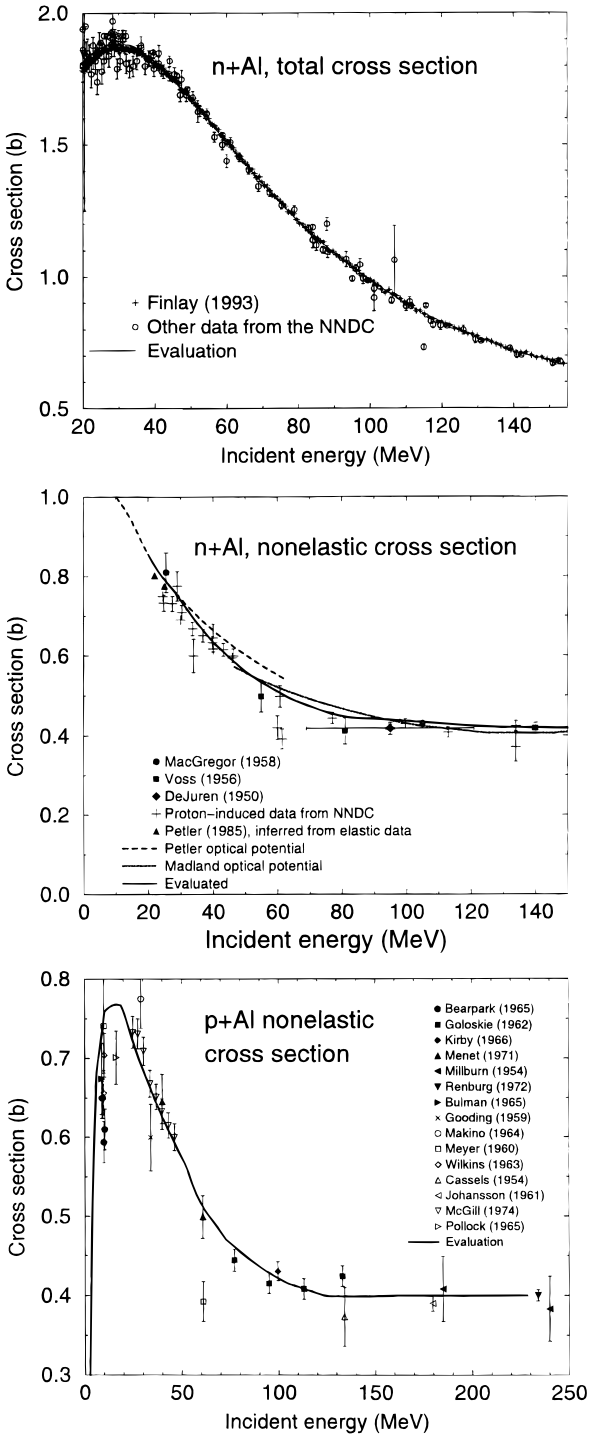

Fig. 28. Comparison of evaluated neutron total cross section and proton and neutron nonelastic cross sections with experimental data[44,77] for Al.

IV.K. The ^{12}C, ^{14}N, ^{16}O, ^{31}P, and ^{40}Ca Evaluations

Evaluated cross sections for these elements were originally developed by one of the authors (M.B.C.) in the LLNL format for neutron and proton radiotherapy applications. The new evaluations, in ENDF-6 format, represent an extension of that earlier work. In addition to their importance in medical applications, these elements are

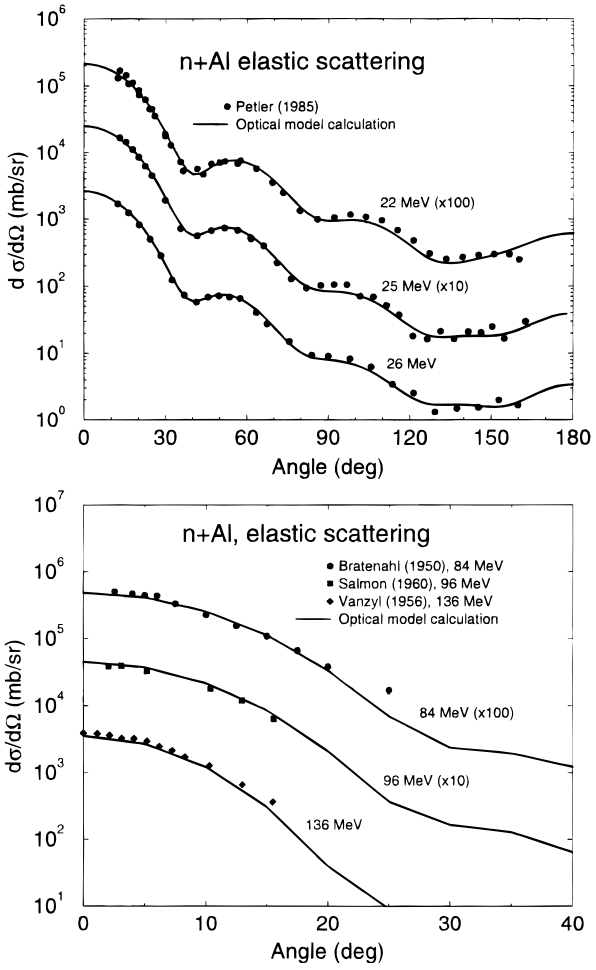

Fig. 29. Comparison of elastic scattering distributions for n + Al, calculated using the optical model, with experimental data.[44]

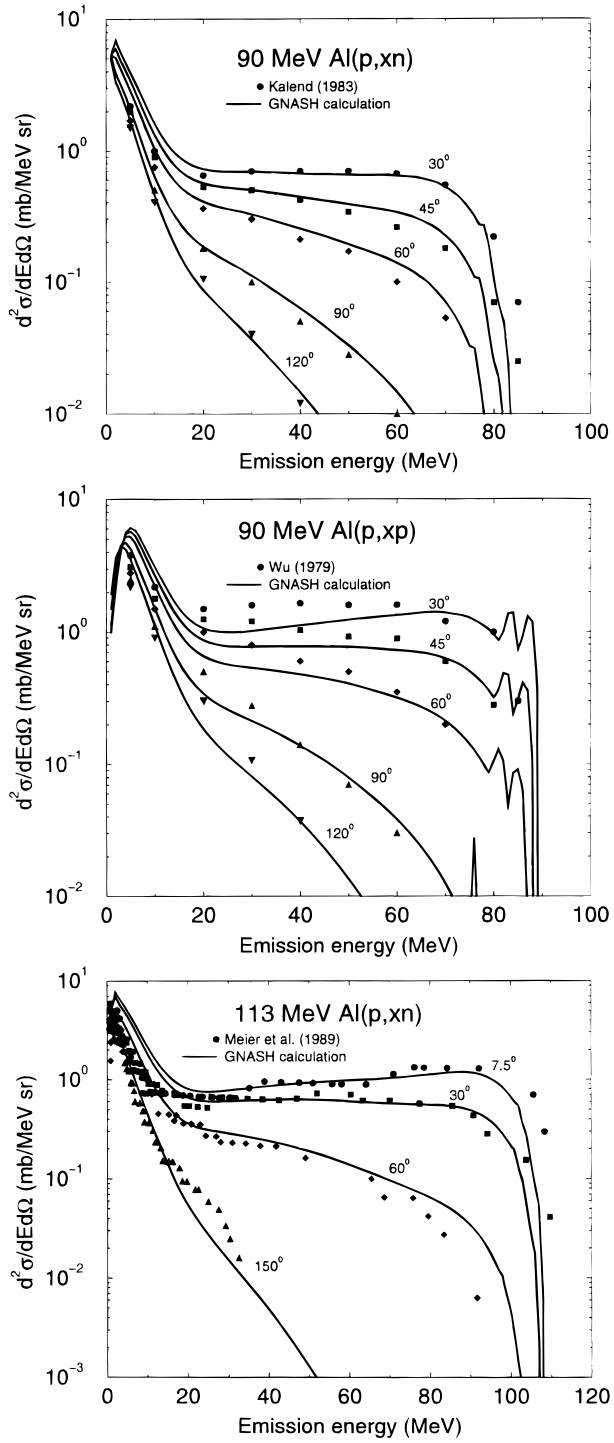

Fig. 30. Comparison of aluminum (p, xn) and (p, xp) double-differential emission spectra with experimental data, at 90 and 113 MeV (Refs. 38, 73, and 74).

also important in accelerator-driven systems (for example, carbon is a beam-stop material, oxygen is present in water and heavy water moderators, and calcium and oxygen are abundant in concrete shielding). The earlier evaluations were documented in detail in Refs. 14, 15, and 43; therefore, only additional details are presented here. The main additions and extensions in the current work were (a) inclusion of nuclide production and recoil energy spectra, (b) inclusion of direct inelastic scattering to low-lying collective states for Ca and inclusion of triton emission for P and Ca, and (c) utilization of the ENDF-6 format and the ENDF/B-VI evaluations below 20 MeV.

There is an important difference in these evaluations compared to the previous LLNL work[14,15] that affects the evaluated kerma coefficient: The present evaluations make use of our new recoil calculational method, described in Sec. III. Since the fractional kerma due to the recoils is significant for light target nuclei, the calculated total kerma coefficients for carbon and oxygen differ (slightly) from our previous results, which were based on energy-balance estimates.

The total kerma coefficients derived from our evaluated microscopic cross sections (in the lab reference frame) are compared with measurements in Sec. V.A, and the agreement is good.

Other minor modifications were made to the earlier carbon and oxygen neutron evaluations. For neutron reactions on carbon, the model calculations were modified at 20- and 23-MeV incident energies to increase the abundance of high-energy alpha preequilibrium emission, resulting in a higher $^{12}C(n,\alpha)^{9}Be$ cross section (40 mb at 20 MeV and 18 mb at 23 MeV). This modification was made to obtain better agreement with the measurement by Stevens[91] and with Axton's evaluation.[92] Also, for oxygen at 20- and 23-MeV neutron energy, the fraction of alpha preequilibrium emission was reduced to be more comparable with the results at 27 MeV, where experimental data exist. The motivation for this modification was to reduce the alpha-particle partial kerma coefficient to compensate for the larger nonelastic recoil kerma coefficient obtained in the present work compared to Ref. 15 so that agreement with total kerma coefficient data in the 20- to 23-MeV region is improved.

IV.L. The Deuterium Evaluation

Deuterium is present in the LANL APT design in the heavy water moderator in the target region.

Our evaluation of the $n + {}^{2}H$ cross sections extends to an incident neutron energy of 200 MeV. The neutron total cross section is based on ENDF/B-VI below 100 MeV and on experimental data between 100 and 200 MeV. Our evaluated total cross section from 10 to 200 MeV is compared to the available experimental database[44] in Fig. 31a.

Several neutron elastic scattering angular distribution measurements exist above 20 MeV, which were fitted with Legendre expansions to obtain integrated cross sections and to establish the evaluated angular distributions. The measurements of Romero et al.,[93] Wang,[94] and Howard et al.[95] as well as the partial distributions of Yountz[96] and Palmieri[97] were especially important for determining the neutron elastic scattering data (Fig. 31b).

The elastic scattering, nonelastic, and $^{2}H(n,2n)^{1}H$ cross sections were determined above 20 MeV in parallel, using the fact that the nonelastic cross section essentially equals the $(n,2n)$ cross section above $E_n \approx$ 1 keV, and the elastic and nonelastic cross sections must sum to the total cross section. We revised the existing ENDF/B-VI $(n,2n)$ cross section at most energies between 10 and 100 MeV to improve the agreement with experimental data. The evaluated $^{2}H(n,2n)^{1}H$ and $n + {}^{2}H$ nonelastic cross sections are compared to measurements[44] in Fig. 32. In the course of evaluating the nonelastic cross section at higher energies, experimental proton reaction cross-section data for ^{2}H were found to be consistent with the neutron nonelastic cross-section measurements above ~20 MeV. The proton reaction cross-section measurements of Carlson et al.[98] are included with the nonelastic data in Fig. 32.

For $p + {}^{2}H$ reactions, we utilized the results of an R-matrix analysis for proton energies up to 4 MeV. We compiled a selection of $p + {}^{2}H$ elastic angular distribution measurements up to ~65 MeV and used the results directly in the evaluation.

We utilized the Faddeev calculations of Sloan[99] at lower energies and the results of our $n + {}^{2}H$ evaluation at higher energies for the $^{2}H(p,2pn)$ cross section, taking advantage of the near equality of the proton and neutron reaction cross sections above 20 MeV. Finally, we evaluated the $^{2}H(p,\gamma)^{3}He$ cross section using experimental data below 2 MeV, assuming equality with the $^{2}H(n,\gamma)^{3}H$ cross section above 4 MeV, with a smooth match at intermediate energies.

IV.M. The ^{1}H Evaluation

Hydrogen is an important element in many applications. It is abundant in water moderators and in plastic materials and is present at the ~10% level (by weight) in human tissue, which makes it an important material in fast-neutron and -proton cancer therapy studies. An accurate evaluation of the total cross section, and the neutron-proton elastic scattering angular distributions is important for determining the kinetic energy imparted to secondary recoil protons, which affects the energy deposited by neutrons in matter (kerma). In addition, the back-angle neutron-proton scattering cross section is an important quantity as it is used as a "standard" to determine neutron fluences.

Prior to the present work, an evaluation by Hale et al. for neutrons on hydrogen existed in the ENDF/B-VI library up to 100 MeV. This evaluation was based on an R-matrix representation of measured data up to 26 MeV and a phase-shift analysis by Arndt at higher energies. However, it has some limitations: The Arndt analysis used was an interim analysis available at the time of the evaluation (1988), and the matching to the R-matrix solution below 26 MeV was rather crude. After the completion of this earlier hydrogen evaluation, a standards committee of the Nuclear Energy Agency (NEA) recommended[100] that for hydrogen, ENDF/B-VI should be used below 20 MeV, but at higher energies, cross sections should be taken from Arndt's more recent VL40 phase-shift solution.[101]

We have implemented this NEA recommendation in a new hydrogen evaluation that extends to 150 MeV in ENDF-6 format. The R-matrix solution from ENDF/B-VI and Arndt's VL40 phase-shift solution were merged at 26 MeV, where a smoother transition could be achieved. Furthermore, the merging was performed in a way that resulted in relatively smooth cross sections

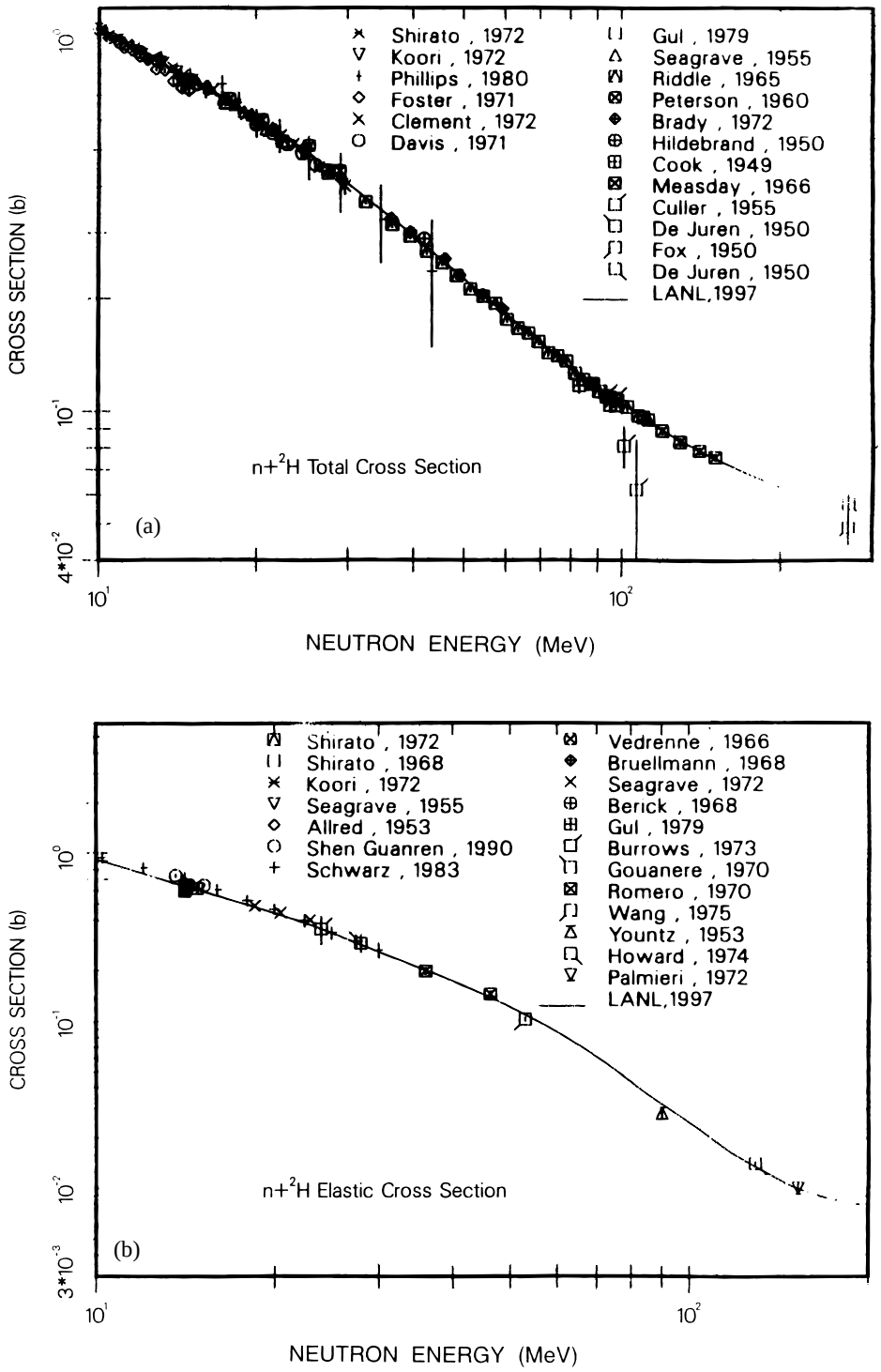

Fig. 31. The evaluated $n + {}^2H$ total cross section and total elastic cross section up to 200 MeV, compared with measurements.[44]

from one region to the other, not just in the total cross section but in the scattering cross sections at different angles. This is described in more detail in Ref. 40.

For proton scattering on hydrogen, a new R-matrix analysis was performed up to 150 MeV, extending a previous evaluation to 100 MeV that was the basis of the existing ENDF/B-VI *p-p* evaluation.

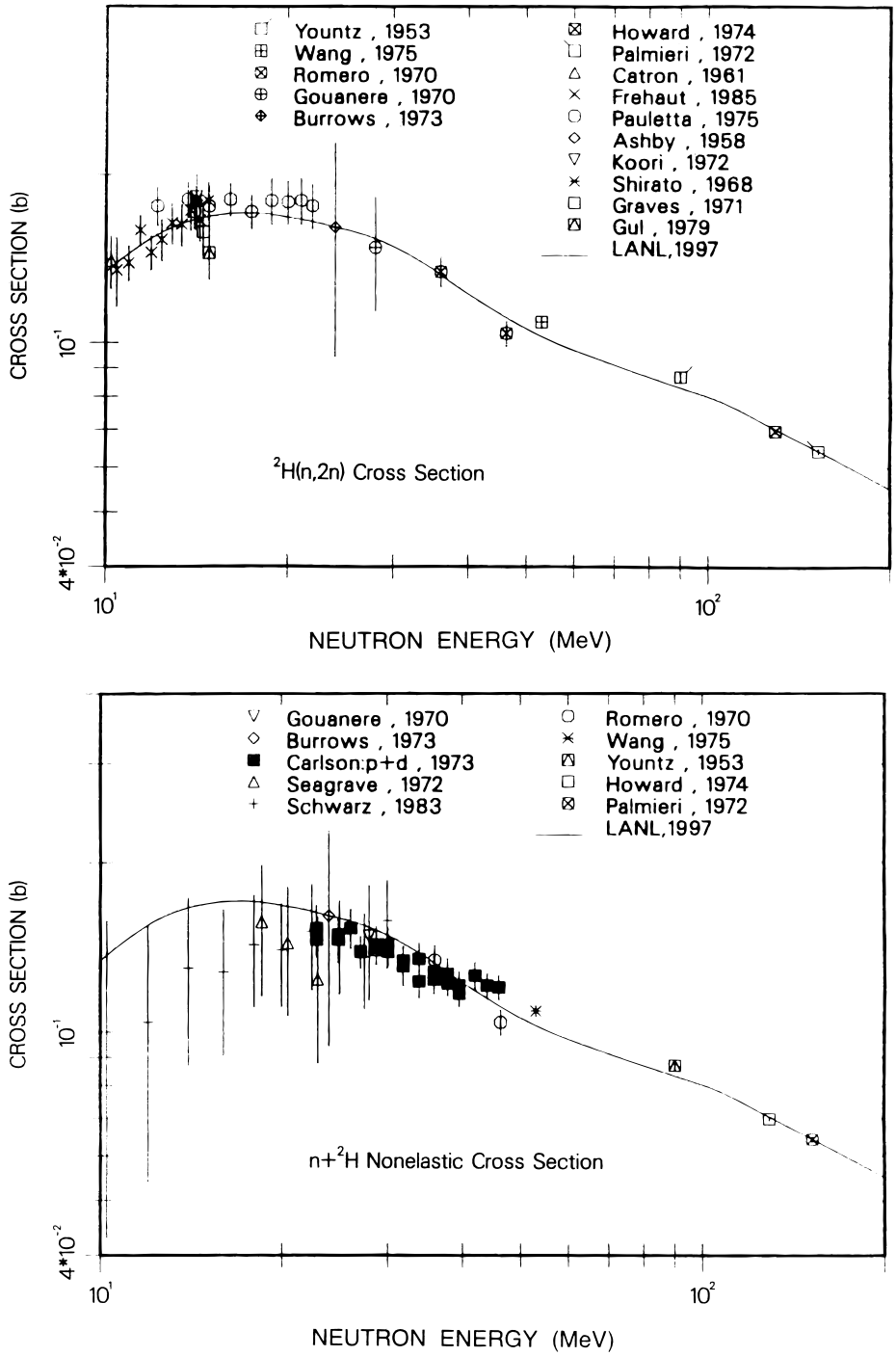

Fig. 32. The evaluated ^{2}H(n,2n) cross section and the n + ^{2}H nonelastic cross section up to 200 MeV, compared with measurements.[44]

V. INTEGRAL BENCHMARKS: TRANSPORT AND ENERGY DEPOSITION

V.A. Kerma Calculations for Energy Deposition

It has been necessary to extend the NJOY Nuclear Data Processing System[102] in a number of ways to process the new 150-MeV neutron and proton data for use by radiation transport codes. One set of extensions is designed to provide accurate kerma coefficients for the determination of radiation heating from neutrons. Heating is important in a variety of applications, including accelerator technologies and calculations of absorbed dose in

radiation therapy. The fluence-to-kerma conversion coefficient, or "kerma coefficient,"[b] is given by the ratio of the kerma (an acronym for kinetic energy released in matter) to the neutron fluence.

The kerma coefficient is proportional to the total energy emitted with secondary charged particles, including the residual nuclei (recoils). A full calculation of radiation heating would have to follow the slowing down (transport) of each particle in the medium, but when charged-particle mean paths are fairly short, folding the kerma coefficient with the neutron fluence can provide a reasonably good approximation to the energy deposition by neutrons in matter. In addition, if total kerma coefficients derived from evaluated cross-section data agree well with measurements, it helps to build confidence in the prediction of energy deposition by a transport code, such as MCNPX, that uses these same data.

V.A.1. Kerma Below 20 MeV

Below 20 MeV, kerma coefficients are calculated from the ENDF/B-VI evaluated cross sections. Following the introduction of the ENDF-6 format, a number of evaluated nuclear data files that contain explicit information on the energies of emitted charged particles have become available. A processing code like NJOY can easily integrate these distributions, thus obtaining kerma coefficients that are directly traceable to the best judgment of the evaluator and that satisfy conservation of energy for all emitted radiations. However, even now, explicit charged-particle distributions are not available for many important materials. Thus, it is necessary to attempt to estimate emitted energies by using kinematics, rough estimates for reaction dynamics, or energy balance. The energy-balance approach takes advantage of the fact that many ENDF-format evaluations give explicit distributions for the emitted neutrons and photons. The energies needed for the kerma coefficient can be obtained by subtracting the average emitted energies for the neutrons and photons from the available energy $(E + Q)$.

V.A.2. Kerma Above 20 MeV

The new high-energy evaluations extend from 20- to 150-MeV neutron energies. These evaluations allow total neutron kerma coefficients to be determined unambiguously because the emission spectra of all secondary charged particles, including heavy $(A > 4)$ recoils, are represented. Since the light-particle ejectile $(A \leq 4)$ angle-integrated spectra are represented in the c.m. frame, NJOY performs a transformation into the lab frame of reference to obtain the partial kerma coefficients for the light particles. Lab-frame angle-integrated spectra are provided for the heavy recoils by making use of the model described in Sec. III and the Appendix. Finally, elastic recoil partial kerma coefficients are determined from the neutron elastic scattering angular distributions after having determined the P_1 component of a Legendre coefficient fit to the highly forward-peaked distributions. Partial kerma coefficients for each type of secondary charged particle are determined using

$$k_{\Phi}^{i} = N\bar{\epsilon}_i \sigma_i^{prod} \quad , \tag{6}$$

where

k_{Φ}^{i} = kerma coefficient of ejectile type i

σ_i^{prod} = inclusive production cross section of ejectile i (b)

$\bar{\epsilon}_i$ = average energy of ejectile i (MeV)

and all these quantities are functions of the incident neutron energy. The factor $N = 9.64853 \times 10^{-15}/M_{\mathrm{A}}$, where M_{A} is the atomic mass of the target in units of u, converts the partial kerma coefficient from units of megaelectron-volts·barn to Système International units of $\mathrm{f\,Gy\,m^2}$ [femto (f) $= 10^{-15}$, gray (Gy) = J/kg].

V.A.3. Comparison with Experiments

In recent years, total kerma coefficients have been measured for a number of elements, particularly those important in medical applications, allowing a test of evaluated nuclear data and the NJOY processing methods. The measurements have been made in two ways: direct determination of the ionization produced by the secondary charged particles and measurements of secondary charged-particle differential cross sections. Both methods involve significant uncertainties; the latter, in particular, require extrapolations for data at unmeasured angles, energies (below detector thresholds), and for elastic and nonelastic recoils to determine the total kerma coefficient.

Figure 33 shows the total kerma coefficients determined by NJOY from the evaluated ENDF data compared with measurements. The discontinuities seen at 20 MeV arise because of the different evaluation methods used in the new high-energy evaluations compared with the older <20-MeV evaluations. In general, the agreement is seen to be good. For C and O, there is a tendency for the ENDF evaluations to overpredict kerma coefficients in the 15- to 20-MeV range. The LAHET results shown were generated with a special version using elastic cross sections from the new ENDF evaluation, and they show reasonable agreement with the full calculation.

Additional comparisons of our calculated kerma coefficients with experimental data relevant to medical applications, such as kerma coefficients for tissue-equivalent A150 plastic, the C/O kerma ratio, and integral results

[b]We follow the notation of the International Commission on Radiation Units and Measurements[40] (ICRU) in using *kerma coefficient* rather than *kerma factor*.

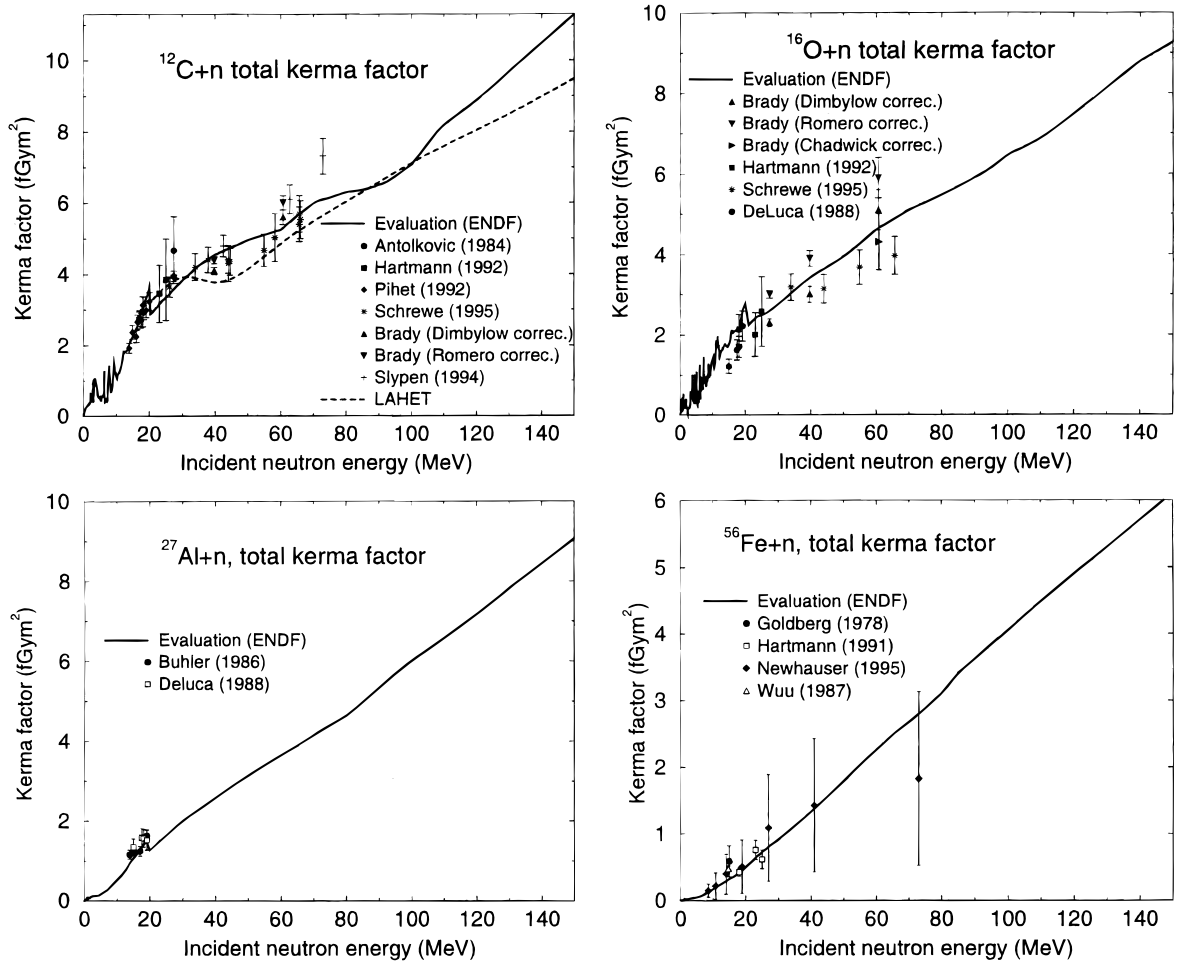

Fig. 33. Calculated kerma coefficients compared with experimental data, for C, O, Al, and Fe. For citations to C and O experimental kerma coefficients, see Refs. 14, 15, and 103; for Al, see Refs. 104 and 105; for Fe, see Refs. 106 through 109.

for kerma in clinical fast-neutron therapy beams, are presented in Ref. 40.

V.B. MCNPX Transport Calculations

V.B.1. MCNPX Overview

A major transport code development effort is under way, primarily in support of the computational needs of the APT program. The main emphases of the MCNPX project are (a) merging existing functionality of the MCNP code[4] and the LAHET Code System[5] (LCS) and (b) improving the physics capabilities of the merged code. One critical aspect of the latter is the use of the new 150-MeV data libraries described in this paper. Therefore, for particle energies above 150 MeV, MCNPX uses intranuclear cascade collision physics to simulate nuclear reactions, but below this energy, the new data libraries are used.

The starting point for the code-merger effort was MCNP Version 4B. The MCNPX code[6] expands the capabilities of MCNP by increasing the set of transportable particles, by making use of the newly evaluated high-energy nuclear data libraries described in this paper, and by incorporating physics models for use where tabular data are unavailable. All of the LAHET nuclear physics modules are included intact in MCNPX, which expands the capabilities of LAHET through the availability of many of the variance-reduction methods of MCNP and through the incorporation of MCNP's very general syntax for specifying geometry, sources, and tallies. The result of this project is a unified, general Monte Carlo transport capability to model a fully coupled cascade of nuclear particles over a wide energy range.

An important requirement of the MCNPX development plan is to implement the necessary tools to model the transport of coupled neutral and charged particles below 150 MeV based on nuclear-data evaluations. The physics capabilities of MCNPX have been upgraded to include the production of secondary charged particles from neutron collisions, using data contained on expanded

continuous-energy neutron cross-section tables. Work is in progress on updating MCNPX to utilize the newly evaluated high-energy data tables for incident protons.

To use the 150-MeV neutron libraries, the routines in MCNP for reading cross sections and for sampling secondary particles have been expanded. The modifications have been managed so that the methods applicable to neutron-induced charged-particle production are very similar to the existing methods for neutron-induced photon production. As in the existing neutron-induced photon algorithm, the code performs a significant amount of pretransport data manipulation. In particular, the list of active particle types for a given problem (specified on the MODE card) is used to expunge unneeded data for the problem. Neutron heating numbers are also modified based on the charged particles to be transported.

At every neutron collision, the possibility of producing secondary charged particles exists. All data used in the sampling process are specific to the collision isotope and are evaluated at the incident neutron energy. The expected weight of a particular charged particle i is $WGT\ \sigma_i^{prod}(E)/\sigma_{tot}(E)$, where WGT is the weight of the incident neutron, $\sigma_i^{prod}(E)$ is the total production cross section of i at incident energy E, and $\sigma_{tot}(E)$ is the total cross section. The number of charged particles produced is an integer (possibly 0) determined by analog sampling. If the code determines that a charged particle will be produced, it then samples the reaction responsible for that particle. There is no correlation between the type of collision and the reactions sampled as being responsible for the various secondary particles that may be produced. While reaction properties are not conserved on an event-by-event basis, they are accurately modeled when averaged over many events.

MCNPX supports several ENDF-6 representations of scattered energy-angle distributions. Specifically, the following representations for secondary charged particles are allowed: tabular energy distributions, angular distributions via equally probable cosine bins, Kalbach systematics for correlated energy-angle distributions, discrete two-body scattering, and n-body phase-space energy distributions. In all cases where necessary, kinematics algorithms currently incorporated in MCNP, which are specific for (neutron-in, neutron-out) physics have been generalized to the (neutron-in, charged-particles-out) situation. In addition, a general c.m. to laboratory conversion technique has been incorporated. As is currently the case for neutron production, all such conversions are based on the assumption of two-body kinematics, which is clearly only an approximation for many high-energy neutron reactions of current interest.

V.B.2. Transport Benchmarks

A number of basic quality assurance tests have been performed for MCNPX. These include the standard set of MCNP test problems[110] and a variety of problems created to ensure internal consistency of the code and agreement with the new data evaluations. Here, we present new benchmark calculations comparing both LAHET and MCNPX with experiments performed at the Japan Atomic Energy Research Institute (JAERI). These calculations particularly test the benefits of using the new evaluated neutron data.

A number of neutron transmission experiments have been performed at the Azimuthally Varying Field Cyclotron facility at the JAERI Takasaki site.[111] Incident 43- or 68-MeV protons impinged on converters consisting of 99.9% enriched ^{7}Li. The $^7\mathrm{Li}(p,n)$ reaction produced nearly monoenergetic neutrons, which were then collimated and allowed to strike iron or concrete targets of various thicknesses. The neutron transmission was measured at several positions relative to the transmission target. Although the neutrons were initially almost monoenergetic in all cases, their actual spectra were measured to allow for more realistic comparison with neutron transport calculations.

Before MCNPX was available, simulations of some of these experiments were performed by Hertel and Evans using the LCS. Reference 112 describes their calculations in detail, and for completeness, it includes sample LAHET and MCNP input files. Calculations were performed using LAHET versions 2.7 and 2.8, which includes a new elastic scattering model. The conclusion of the investigation was that simulations using LAHET version 2.8 were in markedly better agreement with experiment than were simulations using LAHET version 2.7 but that substantial systematic errors remained.

We have now repeated some of Hertel and Evans's calculations using MCNPX, replacing the LAHET transport model with the use of the new evaluated neutron data tables throughout the energy range of the experiments. Specifically, we have calculated the transmission of the quasi-monoenergetic 68-MeV neutron source through 40 cm of iron and predicted the fluence on the axis of the beam and at 20 and 40 cm from the axis for detectors immediately adjacent to the downstream face of the transmission target. A typical result is shown in Fig. 34, which compares the on- and off-axis experimental results with the previous calculations using LAHET versions 2.7 and 2.8 and with the new MCNPX results. There is a dramatic improvement in agreement with the MCNPX calculations using the new evaluated neutron data tables. Furthermore, the large discontinuity seen at 20 MeV in the LAHET calculations, which occurs at the transition to MCNP's use of ENDF/B-VI data libraries, is largely reduced in the MCNPX calculations. The improvement seen in the LAHET 2.8 calculations compared to version 2.7 is due to use of optical model predictions for the total elastic scattering cross section in LAHET 2.8; also, the earlier version used a very simplistic elastic angular distribution formulation, whereas the newer version uses a black-disk diffraction formulation.[113]

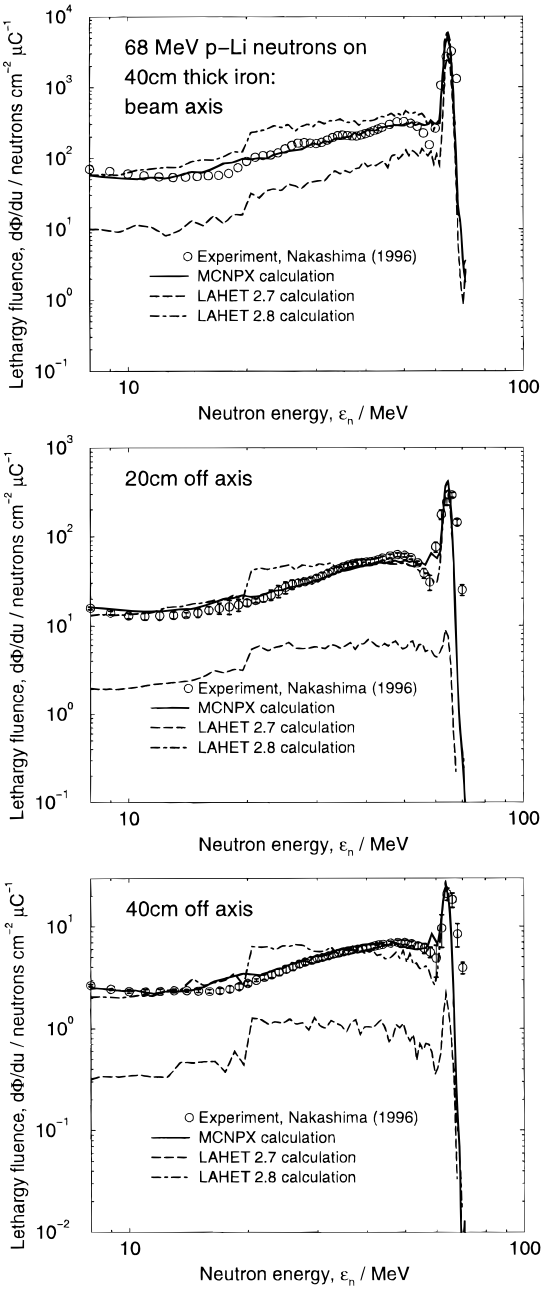

Fig. 34. Comparison of MCNPX calculations of neutron transmission through 40 cm of iron with measurements of Nakashima et al.[111] The neutron source was generated via the 68-MeV ^{7}Li(p,n) reaction. Results are shown for neutron transmission on axis, 20 cm off axis, and 40 cm off axis. Calculations from two versions of the LAHET-MCNP code system are also shown.

Radiation transport simulations using MCNPX with evaluated data up to 150 MeV should be expected to exhibit a discontinuity at 150 MeV, where the transition to INC physics occurs. However, the discontinuities at 150 MeV should be significantly smaller than that previously found at 20 MeV because the INC model is known to be more accurate at higher energies.

VI. SUMMARY

The neutron and proton reaction data that extend up to 150 MeV described in this paper have been evaluated using both nuclear model calculations and experimental data. Extensive benchmarks, both against microscopic cross-section data and integral results for transport and energy deposition, have been performed to validate their accuracy. Good agreement was generally observed.

The evaluations tabulate emission spectra cross sections for neutrons, gamma rays, and light charged particles and, therefore, can be used for calculations of transport. But because they also tabulate such information for heavy charged particles (recoils), the data files can be used for calculations of energy deposition, materials damage, and activation. Therefore, they represent an advance from previous high-energy data evaluations.[1,14–16]

These data can be used in radiation transport calculations for simulations of accelerator-driven systems. They can also be used in medical applications to simulate and optimize absorbed dose in the body by neutron and proton therapy beams. A comprehensive report on this subject will soon be issued by the ICRU (Ref. 40). In applications that involve energies above 150 MeV, a radiation transport code such as MCNPX (Ref. 6) can utilize intranuclear cascade physics methods "on the fly" above 150 MeV and switch to use of these data libraries for particles whose energy has fallen below 150 MeV.

We also note that the library of 150-MeV evaluations described in this work can be augmented with evaluations of other isotopes such as ^{9}Be and ^{238}U from the LANL 100-MeV evaluations[1] developed during the late 1980s, which can also be used in MCNPX transport calculations. This is important for certain applications that make use of beryllium as a (p,xn) neutron source and that use depleted uranium as a spallation target.

These new 150-MeV evaluated cross sections, collectively referred to as the LA150 library, are available via the Internet at http://t2.lanl.gov/data/he.html. In addition, they have been accepted into the ENDF/B-VI library, as Release 6, and are available from the National Nuclear Data Center.[56]

APPENDIX

This Appendix provides kinematic relations for the determination of recoil energy spectra in the laboratory frame of reference, which are built into the GSCAN code. Their usefulness lies in the fact that, while kinematic transformations from c.m. to lab frames are often performed numerically, we show here that they can be performed analytically when the Kalbach angular distribution systematics are applied. This facilitates an exact,

and computationally fast, method for determining recoil energies in the lab frame. Further details can be found in Ref. 20.

The nuclear reaction models considered in this work assume a sequential chain of two-body breakup processes. In each breakup, a composite nucleus, which is moving with a velocity v_a, decays into a light particle (denoted by superscript p) and a heavy recoil (denoted by superscript R).

Suppose the c.m. angular distribution of the light ejectile particle is given by $G(\theta^p,\phi^p)$, where

$$\int G(\theta^p,\phi^p)\,d\Omega = 1 \ ,$$

and the superscript p denotes the particle. Using Kalbach systematics,[36] which represents the angular distribution in terms of hyperbolic sines and cosines and can be rewritten in terms of exponentials, this distribution can be expressed as

$$G(\theta^p,\phi^p) = f_1 \exp(a\cos\theta^p) + f_2 \exp(-a\cos\theta^p) \ , \tag{A.1}$$

where

$$f_1 = \frac{1}{4\pi}\,\frac{a}{e^a - e^{-a}}\,(1 + f_{MSD})$$

and

$$f_2 = \frac{1}{4\pi}\,\frac{a}{e^a - e^{-a}}\,(1 - f_{MSD}) \ , \tag{A.2}$$

where a is the Kalbach-systematics forward-peaking parameter and f_{MSD} is the preequilibrium fraction. The secondary recoil c.m. angular distribution is obtained from the preceding particle result because the recoil moves in the opposite direction with $\theta^R = (\pi - \theta^p)$:

$$G(\theta^R,\phi^R) = f_1 \exp(-a\cos\theta^R) + f_2 \exp(a\cos\theta^R) \ . \tag{A.3}$$

A.I. ANALYTIC METHOD FOR ANGLE-INTEGRATED RECOIL SPECTRUM

In this section, we provide kinematic equations to determine laboratory-frame recoil spectra and average energies. For completeness, we also provide equivalent results for the light-particle ejectiles. Nonrelativistic expressions are currently used.

A.I.A. Light-Particle Ejectile

If θ^p represents the particle c.m. angle, v_l^p, v_c^p, and v_a represent velocities in the lab, c.m., and the c.m.-to-lab boost velocity c.m. motion, then the cosine formula for vector addition of these velocities yields

$$\cos(\theta^p) = \frac{{v_l^p}^2 - v_a^2 - {v_c^p}^2}{2v_a^p v_c^p} = \frac{\epsilon_l^p - \epsilon_a^p - \epsilon_c^p}{m^p v_a v_c^p} \ , \tag{A.4}$$

where

$$\epsilon_l^p = \tfrac{1}{2} m^p {v_l^p}^2$$

$$\epsilon_a^p = \tfrac{1}{2} m^p {v_a^p}^2$$

$$\epsilon_c^p = \tfrac{1}{2} m^p {v_c^p}^2 .$$

The probability for the particle having a lab energy ϵ_l^p is proportional to $G(\theta^p,\phi^p)\sin(\theta^p)d\theta^p$, and since from Eq. (A.4) we have $\sin(\theta^p)d\theta^p = (1/m^p v_a v_c^p)d\epsilon_l^p$, the probability for the particle having a lab energy ϵ_l^p is

$$P(\epsilon_l^p) = \frac{2\pi}{m^p v_a v_c^p}\,G(\theta^p,\phi^p) \tag{A.5}$$

for $|(v_a - v_c^p)| \le v_l^p \le (v_a + v_c^p)$, and zero otherwise. Substituting the expression for $G(\theta^p,\phi^p)$ from Eqs. (A.1) and (A.2), we obtain

$$P(\epsilon_l^p) = \frac{2\pi}{m^p v_a v_c^p}\left[f_1 \exp\left(a\left(\frac{\epsilon_l^p - \epsilon_a^p - \epsilon_c^p}{m^p v_a v_c^p} \right) \right) + f_2 \exp\left(-a\left(\frac{\epsilon_l^p - \epsilon_a^p - \epsilon_c^p}{m^p v_a v_c^p} \right) \right) \right] . \tag{A.6}$$

A.I.B. Heavy Recoil Ejectiles

The probability for recoils having a laboratory energy ϵ_l^R can be obtained in exactly the same way as in Sec. A.I.A. Using the recoil angular distribution given by Eq. (A.3), which is identical to Eq. (A.1) except for the sign reversals in the exponentials, we obtain

$$P(\epsilon_l^R) = \frac{2\pi}{m^R v_a v_c^R}\left[f_1 \exp\left(-a\left(\frac{\epsilon_l^R - \epsilon_a^R - \epsilon_c^R}{m^R v_a v_c^R} \right) \right) + f_2 \exp\left(+a\left(\frac{\epsilon_l^R - \epsilon_a^R - \epsilon_c^R}{m^R v_a v_c^R} \right) \right) \right] , \tag{A.7}$$

for $|(v_a - v_c^R)| \le v_l^R \le (v_a + v_c^R)$, and zero otherwise, where

$$\epsilon_l^R = \tfrac{1}{2} m^R {v_l^R}^2$$

$$\epsilon_a^R = \tfrac{1}{2} m^R {v_a^R}^2$$

$$\epsilon_c^R = \tfrac{1}{2} m^R {v_c^R}^2 .$$

We define recoil velocities v_c^R and v_l^R as previously for the particles.

Equation (A.7) gives the average spectrum of lab recoil energies given a c.m. motion addition boost velocity

v_a and a c.m. recoil velocity v_c^R. In general, however, each of these quantities is given by a distribution of values. The overall lab recoil velocity spectrum can be written as a double integral over these quantities:

$$P(\epsilon_l^R) = \int_{\epsilon_a^R}\int_{\epsilon_c^R=\epsilon_l^R+\epsilon_a^R-2\sqrt{\epsilon_l^R\epsilon_a^R}}^{\epsilon_c^R=\epsilon_l^R+\epsilon_a^R+2\sqrt{\epsilon_l^R\epsilon_a^R}} P_1(\epsilon_a^R)P_2(\epsilon_c^R)\,d\epsilon_a^R\,d\epsilon_c^R \times \left(\frac{2\pi}{m^R v_a v_c^R}\left[f_1\exp\left(-a\left(\frac{\epsilon_l^R-\epsilon_a^R-\epsilon_c^R}{m^R v_a v_c^R}\right)\right) + f_2\exp\left(+a\left(\frac{\epsilon_l^R-\epsilon_a^R-\epsilon_c^R}{m^R v_a v_c^R}\right)\right)\right]\right), \tag{A.8}$$

where $P_1(\epsilon_a^R)$ and $P_2(\epsilon_a^R)$ are the spectra (in energy) of the recoil lab motion energies and the c.m. recoil energies. In the case of isotropic particle emission, this becomes

$$P(\epsilon_l^R)^{\text{isotropy in c.m.}} = \int_{\epsilon_a^R}\int_{\epsilon_c^R=\epsilon_l^R+\epsilon_a^R-2\sqrt{\epsilon_l^R\epsilon_a^R}}^{\epsilon_c^R=\epsilon_l^R+\epsilon_a^R+2\sqrt{\epsilon_l^R\epsilon_a^R}} \times P_1(\epsilon_a^R)P_2(\epsilon_c^R)\,d\epsilon_a^R\,d\epsilon_c^R \times \left[\frac{1}{4\sqrt{\epsilon_a^R\epsilon_c^R}}\right]. \tag{A.9}$$

A simplifying assumption that we currently make is to ignore the distribution of $P_1(\epsilon_a^R)$ and just use an averaged value of ϵ_a^R [i.e., $P_1(\epsilon_a^R) = \delta(\overline{\epsilon_a^R})$].

A.II. ANALYTIC METHOD FOR AVERAGE ENERGY OF RECOIL SPECTRUM

There are some situations where it is useful to have an analytic result for the average lab energies. This quantity provides a useful check on the accuracy of the derived lab spectra and can be used directly to obtain the recoil partial kerma coefficients.

A.II.A. Light-Particle Ejectile

Application of the cosine formula gives ${v_l^p}^2 = {v_c^p}^2 + v_a^2 + 2v_c^p v_a\cos\theta^p$. Using the Kalbach c.m. angular distribution in Eq. (A.1), the average lab particle energy for an initial c.m. energy ϵ_c^p is given by

$$\overline{\epsilon_l^p} = 2\pi\int_0^\pi \frac{1}{2}m^p[{v_c^p}^2 + v_a^2 + 2v_c^p v_a\cos\theta^p] \times G(\theta^p,\phi^p)\sin\theta^p\,d\theta^p\ . \tag{A.10}$$

When substituting the expression for $G(\theta^p,\phi^p)$ from Eq. (A.1), solution of Eq. (A.10) involves solving integrals of the type

$$I_1(a) = \int_0^\pi \exp(a\cos\theta^p)\sin\theta^p\,d\theta^p = \left[\frac{e^a - e^{-a}}{a}\right] \tag{A.11}$$

and

$$I_2(a) = \int_0^\pi \exp(a\cos\theta^p)\cos\theta^p\sin\theta^p\,d\theta^p = \left[\frac{e^a + e^{-a}}{a}\right] - \frac{1}{a^2}[e^a - e^{-a}]\ . \tag{A.12}$$

These equations give the average energy of the particles in the lab as

$$\overline{\epsilon_l^p} = \tfrac{1}{2}m^p({v_c^p}^2 + v_a^2) + f_{MSD}\cdot m^p v_c^p v_a I_2(a)/I_1(a)\ . \tag{A.13}$$

A.II.B. Heavy Recoil Ejectile

The derivation of the recoil average lab energy follows that described in Sec. A.II.A for the ejectile particle. The opposite direction of the c.m. recoil relative to the c.m. particle ejectile simply results in the sign change in the exponentials in Eq. (A.3). With this, the average energy for the lab recoils becomes

$$\overline{\epsilon_l^R} = \tfrac{1}{2}m^R({v_c^R}^2 + v_a^2) + f_{MSD}\cdot m^R v_c^R v_a I_2(-a)/I_1(-a)\ . \tag{A.14}$$

In the limiting case of $a \to 0$ (isotropy), $I_2(-a)/I_1(-a) \to 0$; therefore, this becomes $\overline{\epsilon_l^R} = \tfrac{1}{2}m^R({v_c^R}^2 + v_a^2)$, which can be easily derived for an isotropic c.m. angular distribution. Thus, we see that the average kinetic energies of the recoils have increased through such particle decay processes. The opposite limiting case is also of interest—very forward peaked preequilibrium emission that may occur in primary particle emission—which we can study by considering $a \to$ large and $f_{MSD} = 1$. Here, $I_2(-a)/I_1(-a) \to -1$, and Eq. (A.14) reduces to $\overline{\epsilon_l^R} = \tfrac{1}{2}m^R(v_a - v_c^R)^2$. Thus, preequilibrium emission results in a decrease in the recoil velocities, as discussed earlier.

ACKNOWLEDGMENTS

The authors are grateful to P. M. DeLuca, S. M. Grimes, R. C. Haight, D. G. Madland, P. Moller, E. Pitcher, G. Russell, H. Schuhmacher, and W. B. Wilson, for useful conversations.

REFERENCES

1. P. G. YOUNG, E. D. ARTHUR, M. BOZOIAN, T. R. ENGLAND, G. M. HALE, R. J. LABAUVE, R. C. LITTLE, R. E. MacFARLANE, D. G. MADLAND, R. T. PERRY, and W. B. WILSON, "Transport Data Libraries for Incident Proton and

Neutron Energies to 100 MeV," LA-11753-MS, Los Alamos National Laboratory (1990).

2. M. B. CHADWICK and P. G. YOUNG, "The LA150 Cross Section Evaluations to 150 MeV: ENDF File 1 Documentation and Graphical Representations," Los Alamos National Laboratory (in preparation).

3. V. McLANE, "ENDF-102 Data Formats and Procedures for the Evaluated Nuclear Data File ENDF-6," BNL-NCS-44945, Rev. 2/97, Brookhaven National Laboratory, National Nuclear Data Center (1997).

4. "MCNP—A General Monte Carlo n-Particle Transport Code," Version 4B, LA-12625-M (1997), J. F. BRIESMEISTER, Ed., Los Alamos National Laboratory (1997).

5. R. E. PRAEL and H. LICHTENSTEIN, "Users Guide to LCS: The LAHET Code System," LA-UR-89-3014, Los Alamos National Laboratory (1989).

6. H. G. HUGHES, K. J. ADAMS, M. B. CHADWICK, J. C. COMLY, S. C. FRANKLE, J. S. HENDRICKS, R. C. LITTLE, R. E. PRAEL, L. S. WATERS, and P. G. YOUNG, Jr., "Status of the MCNP™/LCS™ Merger Project," *Proc. Radiation Protection and Shielding Division Topl. Conf.*, Nashville, Tennessee, April 19–23, 1998, p. I-188, American Nuclear Society (1998); see also LA-UR-98-559, Los Alamos National Laboratory (1998).

7. P. G. YOUNG, E. D. ARTHUR, and M. B. CHADWICK, "Comprehensive Nuclear Model Calculations: Theory and Use of the GNASH Code," *Proc. IAEA Workshop Nuclear Reaction Data and Nuclear Reactors—Physics, Design, and Safety*, Trieste, Italy, April 15–May 17, 1996, p. 227, A. GANDINI and G. REFFO, Eds., World Scientific Publishing, Ltd., Singapore (1998).

8. P. G. YOUNG, E. D. ARTHUR, and M. B. CHADWICK, "Comprehensive Nuclear Model Calculations: Introduction to the Theory and Use of the GNASH Code," LA-12343-MS, Los Alamos National Laboratory (1992).

9. J. RAYNAL, "Notes on ECIS94," CEA-N-2772, p. 1, Commissariat à l'Energie Atomique, Saclay, France (1994).

10. O. BERSILLON, "Bruyeres-le-Chatel Laboratory Progress Report," CEA-N-2037, p. 111, Commissariat à l'Energie Atomique, Saclay, France (1978).

11. M. BLANN, H. GRUPPELAAR, P. NAGEL, and J. RODENS, "International Code Comparison for Intermediate Energy Nuclear Data," p. 1, Organization for Economic Cooperation and Development Nuclear Energy Agency, Paris, France (1994).

12. M. B. CHADWICK, P. G. YOUNG, D. C. GEORGE, and Y. WATANABE, *Phys. Rev. C*, **50**, 996 (1994).

13. M. BLANN and M. B. CHADWICK, *Phys. Rev. C*, **57**, 233 (1998).

14. M. B. CHADWICK, L. J. COX, P. G. YOUNG, and A. S. MEIGOONI, "Calculation and Evaluation of Cross Sections and Kerma Factors for Neutrons up to 100 MeV on Carbon," *Nucl. Sci. Eng.*, **123**, 17 (1996).

15. M. B. CHADWICK and P. G. YOUNG, "Calculation and Evaluation of Cross Sections and Kerma Factors for Neutrons up to 100 MeV on ^{16}O and ^{14}N," *Nucl. Sci. Eng.*, **123**, 1 (1996).

16. A. J. KONING, O. BERSILLON, and J.-P. DELAROCHE, *Nucl. Instrum. Methods A*, **414**, 49 (1998).

17. M. HARADA, Y. WATANABE, S. CHIBA, and T. FUKAHORI, *J. Nucl. Sci. Technol.*, **34**, 116 (1997).

18. Y. N. SHUBIN, A. V. IGNATYUK, and V. P. LUNEV, "Nuclear Data and Activation of Heavy Metal Targets in Accelerator Driven Technology," *Proc. Int. Conf. Nuclear Data for Science and Technology*, Trieste, Italy, May 19–24, 1997, p. 1421, G. REFFO, Ed., ENEA, Bologna, Italy (1997).

19. S. PEARLSTEIN, *Health Phys.*, **65**, 185 (1993).

20. M. B. CHADWICK, P. G. YOUNG, R. E. MacFARLANE, and A. J. KONING, "Evaluated Nuclear Data Libraries up to 150 MeV: Method for Calculating Recoils," *Proc. 2nd Int. Conf. Accelerator-Driven Transmutation Technologies and Applications*, Kalmar, Sweden, June 3–7, 1996, p. 483, H. CONDÉ, Ed., Gotab, Stockholm, Sweden (1997).

21. H. FESHBACH, A. KERMAN, and S. KOONIN, *Ann. Phys.*, **125**, 429 (1980).

22. M. B. CHADWICK and P. G. YOUNG, *Phys. Rev. C*, **47**, 2255 (1993).

23. A. J. KONING, "Nuclear Data Evaluation for Accelerator-Driven Systems," *Proc. 2nd Int. Conf. Accelerator-Driven Transmutation Technologies and Applications*, Kalmar, Sweden, June 3–7, 1996, p. 438, H. CONDÉ, Ed., Gotab, Stockholm, Sweden (1997).

24. D. G. MADLAND, "Recent Results in the Development of a Global Medium-Energy Nucleon-Nucleus Optical Model Potential," *Proc. Specialists Mtg. Preequilibrium Reactions*, Semmering, Austria, 1988, NEANDC-245, p. 103, B. STROHMAIER, Ed., Organization for Economic Cooperation and Development Nuclear Energy Agency, Paris, France (1988).

25. S. F. MUGHABGHAB, M. DIVADEENAM, and N. E. HOLDEN, *Neutron Cross Sections*, Academic Press, New York (1981).

26. A. J. KONING, J. J. VAN WIJK, and J.-P. DELAROCHE, "ECISVIEW: An Interactive Toolbox for Optical Model Development," *Proc. Int. Mtg. Nuclear Optical Model up to 200 MeV*, Bruyeres-le-Chatel, France, November 13–15, 1996, p. 111, Organization for Economic Cooperation and Development Nuclear Energy Agency, Paris, France (1996).

27. J.-P. DELAROCHE, Y. WANG, and J. RAPAPORT, *Phys. Rev. C*, **39**, 391 (1989).

28. J. LOHR and W. HAEBERLI, *Nucl. Phys. A* **232**, 381 (1974).

29. C. M. PEREY and F. G. PEREY, *At. Data Nucl. Data Tables*, **17**, 1 (1976).

30. F. D. BECCHETTI and G. W. GREENLEES, *Proc. Conf. Polarization Phenomena in Nuclear Reactions*, p. 682, H. H. BARSCHALL and W. HAEBERLI, Eds., University of Wisconsin Press (1971).

31. L. McFADDEN and G. R. SATCHLER, *Nucl. Phys.*, **84**, 177 (1966).

32. A. J. KONING, O. BERSILLON, and J.-P. DELAROCHE, "Quantum-Mechanical Direct, Pre-Equilibrium and Equilibrium Spectra up to 200 MeV," *Proc. Int. Conf. Nuclear Data for Science and Technology*, Gatlinburg, Tennessee, May 9–13, 1994, p. 545, J. K. DICKENS, Ed., American Nuclear Society (1994).

33. J. KOPECKY and M. UHL, *Phys. Rev. C*, **41**, 1941 (1990).

34. A. V. IGNATYUK, G. N. SMIRENKIN, and A. S. TISHIN, *Sov. J. Nucl. Phys.*, **21**, 255 (1975).

35. H. VONACH, A. PAVLIK, M. B. CHADWICK, R. C. HAIGHT, R. O. NELSON, S. A. WENDER, and P. G. YOUNG, *Phys. Rev. C*, **50**, 1952 (1994).

36. C. KALBACH, *Phys. Rev. C*, **37**, 2350 (1988).

37. A. J. KONING and M. B. CHADWICK, *Phys. Rev. C*, **56**, 970 (1997).

38. M. M. MEIER, D. A. CLARK, C. A. GOULDING, J. B. McCLELLAND, G. L. MORGAN, C. E. MOSS, and W. B. AMIAN, "Differential Neutron Production Cross Sections and Neutron Yields from Stoppling-Length Targets for 113-MeV Protons," *Nucl. Sci. Eng.*, **102**, 310 (1989).

39. M. B. CHADWICK, P. G. YOUNG, P. OBLOZINSKY, and A. MARCINKOWSKI, *Phys. Rev. C*, **49**, R2885 (1994).

40. *Nuclear Data for Neutron and Proton Radiotherapy and for Radiation Protection*, International Commission on Radiation Units and Measurements, Bethesda, Maryland (in preparation).

41. M. BLANN and A. EWART, *Phys. Rev.*, **170**, 1131 (1965).

42. E. GADIOLI, E. GADIOLI ERBA, D. J. PARKER, and J. ASHER, *Phys. Rev. C*, **32**, 1214 (1985).

43. M. B. CHADWICK and P. G. YOUNG, *J. Brachytherapy Int.*, **13**, 89 (1997).

44. V. McLANE, CSISRS experimental nuclear data file, National Nuclear Data Center, Brookhaven National Laboratory (1997), http://www.nndc.bnl.gov/.

45. P. W. LISOWSKI, G. F. AUCHAMPAUGH, M. S. MOORE, G. L. MORGAN, and R. E. SHAMU, *Proc. Symp. Neutron Cross Sections from 10 to 50 MeV*, Upton, New York, May 12–14, 1980, BNL-NSC-51245, p. 301, Brookhaven National Laboratory (1980).

46. R. W. FINLAY, W. P. ABFALTERER, G. FINK, E. MONTEI, T. ADAMI, P. W. LISOWSKI, G. L. MORGAN, and R. C. HAIGHT, *Phys. Rev. C*, **47**, 237 (1993).

47. R. E. SHAMU and P. G. YOUNG, *J. Phys. G*, **19**, L169 (1993).

48. W. T. WAGNER, G. M. CRAWLEY, G. R. HAMMERSTEIN, and H. McMANUS, *Phys. Rev. C.*, **11**, 486 (1975).

49. W. T. WAGNER, G. M. CRAWLEY, and G. R. HAMMERSTEIN, *Phys. Rev. C*, **12**, 757 (1975).

50. E. L. HJORT, F. P. BRADY, J. R. DRUMMOND, B. McEACHERN, J. H. OSBORNE, J. L. ROMERO, D. S. SORENSON, and H. H. K. TANG, *Phys. Rev. C*, **53**, 237 (1996).

51. K. SHIBATA, T. FUKAHORI, S. CHIBA, and N. YAMAMURO, *J. Nucl. Sci. Technol.*, **34**, 1171 (1997).

52. F. S. DIETRICH, W. P. ABFALTERER, R. C. HAIGHT, G. L. MORGAN, F. B. BATEMAN, and R. W. FINLAY, "Recent Measurements of Neutron Total Cross Sections on a Wide Range of Targets from 5 to 600 MeV at LANSCE/WNR," *Proc. Int. Conf. Nuclear Data for Science and Technology*, Trieste, Italy, May 19–24, 1997, p. 402, G. REFFO, Ed., ENEA, Bologna, Italy, Bologna, Italy (1997).

53. J. M. PETERSON, A. BRATENAHL, and J. P. STOERING, *Phys. Rev.*, **120**, 521 (1960).

54. R. E. HILDEBRAND and C. E. LEITH, *Phys. Rev.*, **80**, 842 (1950).

55. P. KIRBY and W. T. LINK, *Can. J. Phys.*, **44**, 1847 (1966).

56. C. L. DUNFORD, Internet connection to the National Nuclear Data Center, Brookhaven National Laboratory (1998), http://www.nndc.bnl.gov/.

57. R. E. PRAEL and M. B. CHADWICK, "Application of Evaluated Nuclear Data in the LAHET Code," *Proc. Int. Conf. Nuclear Data for Science and Technology*, Trieste, Italy, May 19–24, 1997, G. REFFO, Ed., ENEA, Bologna, Italy (1997).

58. A. MARCINKOWSKI, P. DEMETRIOU, and P. E. HODGSON, *J. Phys. G*, **22**, 1219 (1996).

59. A. MARCINKOWSKI, R. W. FINLAY, J. RAPAPORT, P. E. HODGSON, and M. B. CHADWICK, *Nucl. Phys. A*, **501**, 1 (1989).

60. H. VONACH, "Results of Recent Code Comparisons," *Proc. Specialists Mtg. Preequilibrium Reactions*, Semmering, Austria, 1988, NEANDC-245, p. 265, B. STROHMAIER, Ed.,

Organization for Economic Cooperation and Development Nuclear Energy Agency, Paris, France (1988).

61. D. M. SKYRME, *Nucl. Phys.*, **35**, 177 (1962).

62. M. B. CHADWICK and P. G. YOUNG, "Is Meier *et al.*'s LANL 113 MeV W(p,xn) Measurement 50% Too High?," Memo T-2-96-57, Los Alamos National Laboratory (1996).

63. W. A. RICHTER, S. W. STEYN, A. A. COWLEY, J. A. STANDER, J. W. KOEN, R. LINDSAY, G. C. HILLHOUSE, P. E. JULIES, J. J. LAWRIE, J. V. PILCHER, and P. E. HODGSON, *Phys. Rev. C*, **54**, 1756 (1996).

64. A. MARCINKOWSKI, R. W. FINLAY, G. RANDERS-PEHRSON, C. E. BRIENT, J. E. O'DONNELL, and K. STANKIEWICZ, *Nucl. Phys. A*, **402**, 220 (1983).

65. H. SAKAI, K. HOSONO, N. MATSUOKA, S. NAGAMACHI, K. OKADA, K. MAEDA, and H. SHIMIZU, *Nucl. Phys. A*, **344**, 41 (1980).

66. H. GRUPPELAAR and P. NAGEL, "International Nuclear Model and Code Comparison on Pre-Equilibrium Effects," in *Preequilibrium Effects: An International Nuclear Model and Code Comparison*, p. 1, Organization for Economic Cooperation and Development Nuclear Energy Agency, Paris, France (1985).

67. Y. WATANABE, "Continuum (p,xp) Spectra at 14.1 and 26 MeV," *Proc. Int. Conf. Nuclear Data for Science and Technology*, Trieste, Italy, May 19–24, 1997, p. 580, G. REFFO, Ed., ENEA, Bologna, Italy (1997).

68. J. P. DELAROCHE, S. M. EL-KADI, P. P. GUSS, C. E. FLOYD, and R. L. WALTER, *Nucl. Phys. A*, **390**, 541 (1982).

69. A. J. KONING, M. B. CHADWICK, and P. G. YOUNG, "ENDF/B-VI Neutron and Proton Datafiles up to 150 MeV for ^{63}Cu and ^{65}Cu," LA-UR-98-1737, Los Alamos National Laboratory (1998).

70. A. J. KONING, J. P. DELAROCHE, and O. BERSILLON, "Neutron and Proton Data Files up to 150 MeV for 54Fe, 56Fe, 58Ni and 60Ni," ECN-RX-97-047, Netherlands Energy Research Foundation (1997).

71. R. C. HARPER and W. L. ALFORD, *J. Phys. G*, **8**, 153 (1982).

72. R. C. HAIGHT, F. B. BATEMAN, S. M. STERBENZ, M. B. CHADWICK, P. G. YOUNG, S. M. GRIMES, O. A. WASSON, P. MAIER-KOMOR, and H. VONACH, "The ^{58,60}Ni(x,α) Reactions from Threshold to 50 MeV," *Proc. Int. Conf. Nuclear Data for Science and Technology*, Trieste, Italy, May 19–24, 1997, p. 603, G. REFFO, Ed., ENEA, Bologna, Italy (1997).

73. J. R. WU, C. C. CHANG, and H. D. HOLMGREN, *Phys. Rev. C*, **19**, 698 (1979).

74. A. M. KALEND, B. D. ANDERSON, A. R. BALDWIN, R. MADEY, J. W. WATSON, C. C. CHANG, H. D. HOLMGREN, R. W. KOONTZ, J. R. WU, and H. MACHNER, *Phys. Rev. C*, **28**, 105 (1983).

75. W. A. RICHTER, A. A. COWLEY, R. LINDSAY, J. J. LAWRIE, S. V. FORTSCH, J. V. PILCHER, R. BONETTI, and P. E. HODGSON, *Phys. Rev. C*, **46**, 1030 (1992).

76. E. D. ARTHUR and P. G. YOUNG, *Proc. Symp. Neutron Cross Sections from 10 to 50 MeV*, Brookhaven National Laboratory, Upton, New York, May 12–14, 1980, BNL-NSC-51245, p. 731, M. R. BHAT, Ed., Brookhaven National Laboratory, Upton, New York (1980).

77. R. F. CARLSON, *At. Data Nucl. Data Tables*, **63**, 93 (1996).

78. F. E. BERTRAND and R. W. PEELLE, *Phys. Rev.*, **8**, 1045 (1973).

79. Y. WATANABE, Kyushu University, Japan, Private Communication to M.B.C. (1998).

80. R. MICHEL, Private Communication to M.B.C. (1997); available from the Nuclear Energy Agency; http://www.nea.fr.

81. R. MICHEL and P. NAGEL, "International Codes and Model Intercomparison for Intermediate Energy Activation Yields," NSC/DOC(97)-1, p. 1, Organization for Economic Cooperation and Development Nuclear Energy Agency, Paris, France (1997); see also *Proc. Specialists' Mtg. Intermediate Energy Nuclear Data*, Issy-les-Moulineaux, France, May 30–June 1, 1994.

82. R. ALARCON and J. RAPAPORT, *Nucl. Phys. A*, **458**, 502 (1986).

83. H. KITAZAWA and Y. HARIMA, *Proc. Int. Conf. Nuclear Data for Science and Technology*, Mito, Japan, May 30–June 3, 1988, p. 473, Japan Atomic Energy Research Institute, Mito, Japan (1988).

84. H. KALKA, M. TORJMAN, and D. SEELIGER, *Phys. Rev. C*, **40**, 1619 (1989).

85. M. LAMBERT, S. BENCK, I. SLYPEN, V. CORCALCIUC, and J. P. MEULDERS, "Comparison of Fast Neutron Induced Light Charged Particle Production Cross Sections for Si and Al," *Proc. Int. Conf. Nuclear Data for Science and Technology*, Trieste, Italy, May 19–24, 1997, p. 1516, G. REFFO, Ed., ENEA, Bologna, Italy (1997).

86. F. B. BATEMAN, R. C. HAIGHT, S. M. STERBENZ, M. B. CHADWICK, P. G. YOUNG, H. VONACH, and S. M. GRIMES, "Silicon (n,Charge Particle) Reactions up to 50 MeV," *Bull. Am. Phys. Soc.*, **43**, 1229 (1998).

87. W. P. ABFALTERER, R. W. FINLAY, S. M. GRIMES, and V. MISHRA, *Phys. Rev. C*, **47**, 1033 (1993).

88. J. S. PETLER, M. S. ISLAM, R. W. FINLAY, and F. S. DIETRICH, *Phys. Rev. C*, **32**, 673 (1985).

89. S. BENCK, I. SLYPEN, J. P. MEULDERS, V. CORCALCIUC, M. B. CHADWICK, P. G. YOUNG, and A. J. KONING, *Phys. Rev. C*, **58**, 1558 (1998).

90. A. PAVLIK, H. HITZENBERGER-SCHAUER, H. VONACH, M. B. CHADWICK, R. C. HAIGHT, R. O. NELSON, and P. G. YOUNG, *Phys. Rev. C*, **57**, 2416 (1998).

91. A. P. STEVENS, PhD Thesis, University of Cape Town (1976).

92. E. J. AXTON, "An Evaluation of Kerma in Carbon and the Carbon Cross Sections," NISTIR 4838, National Institute of Standards and Technology (1992).

93. J. L. ROMERO, J. A. JUNGERMAN, F. P. BRADY, W. J. KNOX, and Y. ISHIZAKI, *Phys. Rev. C*, **2**, 2134 (1970).

94. J. C. W. WANG, *Diss. Abs. B*, **35**, 3511 (1975).

95. V. J. HOWARD, J. A. EDINGTON, S. S. DASGUPTA, I. M. BLAIR, B. E. BONNER, F. P. BRADY, M. W. McNAUGHTON, and N. M. STEWART, *Nucl. Phys. A*, **218**, 140 (1974).

96. B. L. YOUNTZ, "Elastic and Inelastic Scattering of 90-MeV Neutrons by Deuterons," UCRL-2307, University of California Lawrence Radiation Laboratory (1953).

97. J. N PALMIERI, *Nucl. Phys. A*, **188**, 72 (1972).

98. R. F. CARLSON, P. DOHERTY, I. MARGAZIOTIS, S. V. TIN, and W. T. H. VAN OERS, *Lett. Nuovo Cim.*, **8**, 319 (1973).

99. I. H. SLOAN, *Nucl. Phys. A*, **168**, 211 (1971).

100. H. CONDÉ, *Nuclear Data Standards for Nuclear Measurements*, NEANDC-311"U"/INDC(SEC)-101, H. CONDÉ, Ed., Organization for Economic Cooperation and Development Nuclear Energy Agency, Paris, France (1992).

101. R. A. ARNDT, J. S. HYSLOP, and L. D. ROPER, *Phys. Rev. D*, **35**, 128 (1987).

102. R. E. MacFARLANE, "The NJOY Nuclear Data Processing System, Version 91," LA-12740-M, Los Alamos National Laboratory (1994).

103. U. J. SCHREWE, W. D. NEWHAUSER, H. J. BREDE, and P. M. DELUCA, Jr., "Neutron Kerma Factor Measurements in the Energy Range Between 5 MeV and 66 MeV," *Proc. Int. Conf. Nuclear Data for Science and Technology*, Trieste, Italy, May 19–24, 1997, p. 1643, G. REFFO, Ed., ENEA, Bologna, Italy (1997).

104. G. BÜHLER, H. MENZEL, H. SCHUHMACHER, G. DIETZE, and S. GULDBAKKE, *Phys. Med. Biol.*, **31**, 601 (1986).

105. P. M. DeLUCA, Jr., H. H. BARSCHALL, Y. SUN, and R. C. HAIGHT, *Radiat. Prot. Dosim.*, **23**, 27 (1988).

106. E. GOLDBERG, D. R. SLAUGHTER, and R. H. HOWELL, "Experimental Determination of Kerma Factors at E_n = 15 MeV," UCID-17789, Lawrence Livermore Laboratory (1978).

107. C. L. HARTMANN, PhD Thesis, University of Wisconsin (1991).

108. W. D. NEWHAUSER and U. J. SCHREWE, *At. Data Nucl. Data Tables*, **65**, 37 (1997).

109. C. WUU and L. MILAVICKAS, *Med. Phys.*, **14**, 1007 (1987).

110. R. C. BROCKHOFF and J. S. HENDRICKS, "A New MCNP™ Test Set," LA–12839, Los Alamos National Laboratory (1994).

111. H. NAKASHIMA, N. NAKAO, S. TANAKA, T. NAKAMURA, K. SHIN, S. TANAKA, H. TAKADA, S. MEIGO, Y. NAKANE, Y. SAKAMOTO, and M. BABA, "Transmission Through Shields of Quasi-Monoenergetic Neutrons Generated by 43- and 65-MeV Protons—II: Iron Shielding Experiment and Analysis for Investigating Calculational Method and Cross-Section Data," *Nucl. Sci. Eng.*, **124**, 243 (1996).

112. N. E. HERTEL and T. M EVANS, "Benchmarking the LAHET Elastic Scattering Model for APT Design Applications," ERDA Final Report, Task Order 96-081, Georgia Institute of Technology (1997).

113. R. E. PRAEL and D. G. MADLAND, "A Nucleon-Nucleus Elastic Scattering Model for LAHET™," *Proc. Topl. Mtg. Radiation Protection and Shielding*, No. Falmouth, Massachusetts, April 21–25, 1996, p. 251, American Nuclear Society (1996).